A COMBINED-MODE FOURIER ANALYSIS OF DG METHODS FOR LINEAR PARABOLIC PROBLEMS[*]

MOHAMMAD ALHAWWARY[†] AND ZHIJIAN WANG[†]

Abstract. Fourier analysis has been shown to provide valuable insight into the dispersion and dissipation characteristics of numerical schemes for PDEs. Applying Fourier analysis to discontinuous Galerkin (DG) methods results in an eigenvalue problem with multiple eigenmodes. It was often relied on one of these modes, the so-called physical-mode, for studying the dispersion and dissipation behavior. The effect of the other modes was considered spurious and typically neglected. Recently, a new approach, the combined-mode approach, was proposed for the linear wave equation, in which all modes are considered. In this paper, we apply the combined-mode approach to a number of DG methods for diffusion. We show that for the linear parabolic heat equation, the physical-mode behavior is completely different than the exact diffusion, over a wide range of wavenumbers, and sometimes nondissipative. In contrast, the combined-mode behavior is more consistent and sufficiently accurate in comparison with the exact diffusion for the whole wavenumber range. This approach also revealed that short time and long time diffusion behaviors are very different for high-order multi–degrees of freedom methods. Additionally, using this approach we conduct a comparative diffusion analysis between a number of popular DG methods for diffusion in one and two dimensions. We also provide a study on the influence of the penalty parameter on their behavior. The considered methods include the symmetric interior penalty, Bassi and Rebay, and the local and compact DG methods. The results are verified numerically through several test cases.

Key words. combined-mode Fourier analysis, linear diffusion analysis, local discontinuous Galerkin, compact discontinuous Galerkin, Bassi and Rebay, interior penalty

AMS subject classifications. 65M60, 65M70, 76M10, 76R50, 76F99

DOI. 10.1137/20M1316962

1. Introduction. The numerical discretization of PDEs results in numerical dispersive and dissipative errors even for nondispersive and nondissipative models. These types of errors are typically analyzed in simplified settings using Fourier or von Neumann analysis [38, 22, 1, 17, 41]. Although strictly applied to linear equations with periodic boundary conditions, it has been shown that this technique can provide valuable insights about the numerical dispersive and dissipative errors for nonlinear models [29, 37, 2]. In addition, for many applications involving convective-diffusive systems, such as the Navier–Stokes equations at high Reynolds numbers, controlling the numerical dissipation is essential to ensure stability and robustness. For such complex applications, high-order discontinuous Galerkin (DG) methods have emerged as a suitable candidate overcoming some of the shortcomings of other discretization methods.

The DG method, originally introduced by Reed and Hill [32] to solve the neutron transport equation, is arguably the most popular method in the class of adaptive high-order methods on unstructured grids [39, 24]. LaSaint and Raviart [26] performed an error analysis for the DG method. It was then further developed for convection-

[†]Department of Aerospace Engineering, University of Kansas, Lawrence, KS 66045 USA (mhawwary@ku.edu, zjw@ku.edu).

dominated problems and fluid dynamics by many researchers; see, for example, [11, 5, 21, 35] and references therein.

For elliptic problems, a number of formulations have been developed, such as the symmetric interior penalty (**SIPG**) [13, 20], Bassi and Rebay (**BR1** [5], **BR2** [6]), and the local DG (**LDG**) [10] and compact DG (**CDG**) [30] methods. These DG discretization methods often include a penalty parameter that is utilized to ensure the stability. In the work of Arnold et al. [3], the theoretical convergence, stability, and consistency of several methods have been studied through a unified framework. In addition, Castillo [8] has conducted a comparative study for a number of interior penalty methods and the **LDG** method for elliptic problems with emphasis on the influence of method parameters on the condition number. Shahbazi [34] and Epshteyn and Rivière [14] have provided more guidance for choosing the penalty parameter for the **SIPG** method to ensure the stability and coercivity. Recently, Quaegebeur et al. [31] have provided the minimum values necessary for stability of a given energy stable flux reconstruction scheme (ESFR) using either **SIPG** or **BR2** methods, following the proofs [9] for the **LDG** method. The stability of **BR1** formulation for the DG spectral element method (DGSEM) in energy stable split forms on Gauss–Lobatto points has been studied by Gassner et al. [18].

Despite all these efforts, little insight into the penalty parameter influence on the diffusion error exists. Moreover, the relative efficiency and diffusion properties of different schemes with respect to the wavenumber were not studied in the literature in great detail. In fact, the application of Fourier analysis to parabolic and diffusion problems with high-order methods is not as popular as it is for advection-dominated problems; see, for example, [42, 25, 43, 19] to name a few. In [23], Huynh has conducted a Fourier analysis for several viscous flux formulations in the context of flux reconstruction (FR) space discretization schemes in addition to the recovery method of Van Leer and Nomura [27]. Kannan and Wang [25] have studied a number of viscous flux formulations for the Navier–Stokes equations using a p-multigrid spectral volume (SV) solver.

In all the previous Fourier analysis studies for high-order DG methods, only one eigenmode was considered in order to analyze their performance, that is, the so-called the *physical-mode* [22]. However, as has been shown previously [2] for the wave equation, the *physical-mode* is only accurate in the low wavenumber range (up to half the wavenumber range for the advection case). On the other hand, for the heat equation, we show in this paper that the *physical-mode* is even more restricted to a very small subset of the wavenumber range, which makes it only relatively accurate up to six points per wavelength (or up to one-third of the wavenumber range). Therefore, in this paper we utilize the *combined-mode* analysis in order to accurately analyze the diffusion properties of several popular DG methods for diffusion. We note that with possibly the same observation and goal, another approach was recently introduced by Fernandez et al. [15] in which they investigate the behavior of hybridized DG methods for linear advection-diffusion in the limit of short time simulation, i.e., $t \to 0$. While in their approach they have adopted the same idea of considering all eigen-modes, the *combined-mode* analysis is more general since it is not restricted only to short time simulations but can describe the behavior of a high-order scheme for any point in time. Hence, *combined-mode* analysis can also describe the evolution of the diffusion error with time and distinguish short and long time simulations.

We start this article by introducing the considered methods in a unified form in section 2 that further enlightens the analysis. We then conduct the semidiscrete analysis using both the classical Fourier analysis approach and the *combined-mode*

analysis approach, in section 3. In this regard, we compute the minimum values of the penalty parameters for the von Neumann stability. Afterward, the diffusion properties of all schemes are studied using the *combined-mode* analysis in a comparative manner. In addition, we investigate the effects of the penalty parameters and polynomial orders on the diffusion behavior in one dimension (1D) and two dimensions (2D). The results agree very well with the numerical simulation of a viscous Burgers turbulence case in section 4, as well as other numerical verification cases. Finally, section 5 summaries the results and conclusions.

In this paper, matrices are denoted by either capitalized bold letters or bold math calligraphy letters both with an underscore, vectors are denoted by bold letters, and scalars are denoted by plain letters. The columns of a matrix $\underline{\boldsymbol{\mathcal{A}}} \in \mathbb{C}^{m \times n}$ are denoted by $\boldsymbol{A}_j \in \mathbb{C}^m$, $j = 1, \ldots, n$. The scalar entries of the matrix are denoted by $A_{ij} \in \mathbb{C}$ such that $\boldsymbol{A}_j = [A_{1j}, \ldots, A_{mj}]$.

2. The DG method.

2.1. Problem definition.
In this section we present the basic formulation of the DG method for a 1D linear parabolic heat equation of the form

$$(2.1) \qquad \frac{\partial u}{\partial t} - \gamma \frac{\partial^2 u}{\partial x^2} = 0, \quad x \in \mathcal{D}, \quad t > 0,$$

with periodic boundary conditions, where $u(x, t)$ is the solution in the physical domain, $\mathcal{D}$, and γ is a positive constant representing the diffusivity coefficient. By introducing an auxiliary variable $\Theta(x, t) = \partial u / \partial x$, the model second-order equation (2.1) can be written as a system of first-order equations:

$$(2.2a) \qquad \Theta = \frac{\partial u}{\partial x},$$

$$(2.2b) \qquad \frac{\partial u}{\partial t} = \gamma \frac{\partial \Theta}{\partial x}.$$

2.2. DG method for linear parabolic problems.
In the DG framework, the domain $\mathcal{D}$ in 1D is discretized into N_e of nonoverlapping elements, $\Omega_e = \left[x_{e-1/2}, x_{e+1/2} \right]$, such that $\mathcal{D} = \cup_{e=1}^{N_e} \Omega_e$ and each element has a width of h_e and a center point x_e. In addition, DG assumes a reference element with local coordinate $\xi \in [-1, 1]$ and defines a linear mapping between a physical and a reference element of the form

$$(2.3) \qquad x = x_e + \frac{\xi \, h_e}{2}$$

and the Jacobian of the mapping in Ω_e

$$(2.4) \qquad J_e = \frac{\mathrm{d}x}{\mathrm{d}\xi} = \frac{h_e}{2}.$$

On element Ω_e, the solution is approximated by a polynomial $u^e(x, t)$ of degree p in space, i.e., $u^e \in \mathcal{P}^p$, which is a finite-dimensional space of polynomials of degree at most $p \geq 1$. In addition, DG approximates Θ by Θ^e, a polynomial that belongs to the same solution space of $\mathcal{P}^p$ in 1D, whereas for a d-dimensional space $\Theta^e \in [\mathcal{P}^p]^d$. Following [10, 3], the DG formulation is obtained by introducing test functions $v, \psi \in$

$\mathcal{P}^p$ and integrating the system of (2.2) over element Ω_e,

$$(2.5a) \qquad \int_{\Omega_e} \Theta^e \upsilon \, dx = \left[\hat{u} \, \upsilon \right]_{x_{e-1/2}}^{x_{e+1/2}} - \int_{\Omega_e} \frac{\partial \upsilon}{\partial x} u^e \, dx \qquad \qquad \forall \, \upsilon \in \mathcal{P}^p,$$

$$(2.5b) \qquad \int_{\Omega_e} \frac{\partial u^e}{\partial t} \psi \, dx = \gamma \left(- \int_{\Omega_e} \Theta^e \frac{\partial \psi}{\partial x} \, dx + \left[\hat{\Theta} \psi \right]_{x_{e-1/2}}^{x_{e+1/2}} \right) \qquad \forall \, \psi \in \mathcal{P}^p,$$

where $\hat{u}, \hat{\Theta}$ represents the numerical approximations of u, Θ at interfaces. The definition of the numerical functions $\hat{u}, \hat{\Theta}$ at the interfaces has been studied in several papers [7, 3, 27]. In this report we investigate several well-known DG formulations for the diffusion terms, namely, **BR1** [5], **BR2** [6], **LDG** [10], **CDG** [30], and **SIPG** [20].

For the purpose of studying these methods, we introduce some useful operators. Define the average operator at an interface $\{\!\{\ldots\}\!\}$ and the jump operator across that interface $[\![\ldots]\!]$ for any quantity q as follows:

$$(2.6) \qquad \{\!\{q\}\!\} = \frac{1}{2} \left(q^- + q^+ \right), \quad [\![q]\!] = q^+ \boldsymbol{n}^+ + q^- \boldsymbol{n}^-,$$

where $\boldsymbol{n}^- = -\boldsymbol{n}^+$ are the unit normal vectors and $(.)^- \& (.)^+$ denote the interface values of any quantity associated with the two elements sharing the interface in which $\boldsymbol{n}^-$ points outward of the element associated with $(.)^-$. In this article, we always consider the current element to be $\Omega_e = \Omega^-$.

In order to unify the formulation of different DG methods for diffusion, Arnold et al. [3] utilized the *primal form* of the equations. For the first equation (2.5a), perform integration by parts once again on the second integral on the right-hand side to get

$$(2.7) \qquad \int_{\Omega_e} \Theta^e \, \upsilon \, dx = \left[(\hat{u} - u^e) \, \upsilon \right]_{x_{e-1/2}}^{x_{e+1/2}} + \int_{\Omega_e} \frac{\partial u^e}{\partial x} \, \upsilon \, dx.$$

By selecting $\upsilon = \partial \psi / \partial x$, we then substitute the above equation into (2.5b) and rearrange to arrive at the *primal formulation*

$$(2.8) \quad \int_{\Omega_e} \frac{\partial u^e}{\partial t} \psi \, dx = \gamma \left(\left[\hat{\Theta} \, \psi \right]_{x_{e-1/2}}^{x_{e+1/2}} - \int_{\Omega_e} \frac{\partial u^e}{\partial x} \frac{\partial \psi}{\partial x} \, dx - \left[(\hat{u} - u^e) \frac{\partial \psi}{\partial x} \right]_{x_{e-1/2}}^{x_{e+1/2}} \right).$$

For a standard element $\Omega_s = [-1, 1]$, the solution polynomial u^e can be constructed as a weighted sum of some specially chosen local basis functions $\phi \in \mathcal{P}^p$ defined on the interval $[-1, 1]$,

$$(2.9) \qquad u^e(\xi, t) = \sum_{j=0}^{p} U_j^e(t) \, \phi_j(\xi),$$

where the coefficients U_j^e are the unknown degrees of freedom (DOFs). In a DG formulation, ϕ is chosen to be an orthogonal Legendre polynomial for both test and basis functions, i.e., $\psi = \phi$. As a result, (2.8) constitutes a $p+1$ system of equations for the unknown DOFs $U_j^e, j = 0, \ldots, p$. The system of equations for Ω_s can be written as

$$(2.10) \qquad \begin{aligned} \left(J_e \frac{1}{\gamma} \right) M_{ll} \frac{\partial U_l^e}{\partial t} &= \left[\hat{\Theta} \, \phi_l \right]_{-1}^{1} - \frac{1}{J_e} \sum_{j=0}^{p} S_{lj} U_j^e \\ &\quad - \left[(\hat{u} - u^e) \frac{\partial \phi_l}{\partial \xi} \right]_{-1}^{1}, \qquad l = 0, \ldots, p, \end{aligned}$$

TABLE 1
Definitions of the numerical fluxes for DG methods.

Method	$\hat{u}$	$\hat{\Theta}$
BR1	$\{\!\{u^e\}\!\}$	$\{\!\{\Theta^e\}\!\}$
stabilized **BR1**	$\{\!\{u^e\}\!\}$	$\{\!\{\Theta^e\}\!\} - \alpha^{br1}(\llbracket u \rrbracket)$
BR2	$\{\!\{u^e\}\!\}$	$\{\!\{\nabla u^e\}\!\} - \alpha^{br2}(\llbracket u \rrbracket)$
SIPG	$\{\!\{u^e\}\!\}$	$\{\!\{\nabla u^e\}\!\} - \alpha^{sipg}(\llbracket u \rrbracket)$
LDG	$\{\!\{u^e\}\!\} - \beta_f \llbracket u \rrbracket$	$\{\!\{\Theta^e\}\!\} + \beta_f \llbracket \Theta^e \rrbracket - \alpha^{ldg}(\llbracket u \rrbracket)$
CDG	$\{\!\{u^e\}\!\} - \boldsymbol{\beta}_f \llbracket u \rrbracket$	$\{\!\{\boldsymbol{\Theta}_f^e\}\!\} + \boldsymbol{\beta}_f \llbracket \boldsymbol{\Theta}_f^e \rrbracket - \boldsymbol{\alpha}^{cdg}(\llbracket u \rrbracket)$

where S_{lj}, M_{ll} are constant matrices given by

$$(2.11) \qquad S_{lj} = \int_{-1}^{1} \frac{\partial \phi_l}{\partial \xi} \frac{\partial \phi_j}{\partial \xi} \mathrm{d}\xi, \quad M_{ll} = \int_{-1}^{1} \phi_l \phi_l \mathrm{d}\xi$$

and can be found in Appendix A.

2.3. Numerical flux formulations. In this section, we introduce the numerical flux formulations considered in this work. We also highlight some similarities and equivalence between them.

Table 1 summaries the definitions of the numerical fluxes for each method considered in this work in a unified form similar to [3].

In 1D, $\nabla u^e = \partial/\partial x$ and $\beta_f \in \mathbb{R}$, while in 2D, $\boldsymbol{\beta}_f \in \mathbb{R}^2$ is a vector. The penalty/stabilization term $\alpha(\llbracket u \rrbracket)$ can be written in a general form as

$$(2.12) \qquad \alpha(\llbracket u \rrbracket) = \eta_f \frac{C(\mathrm{p})}{h_f} \llbracket u \rrbracket_f,$$

and $\eta_f \in \mathbb{R}$ is the penalty parameter for interface f, h_f is a carefully chosen length-scale, and $C(\mathrm{p})$ is a function of p. The face f is an interior face, and since we are interested in interior schemes with periodic boundary conditions, these definitions in Table 1 suffice. In 1D, it is customary to choose $h_f = h_e$ as a suitable length-scale.

Considering one of these flux formulations and applying it to (2.10) results in a system of equations of the form

$$(2.13) \qquad \left(\frac{h_e^2}{\gamma}\right) \frac{\partial \mathbf{U}^e}{\partial t} = \underline{\boldsymbol{\mathcal{L}}} \mathbf{U}^e + \sum_{j=1}^{N_{nbe}} \left(\underline{\boldsymbol{\mathcal{K}}}^{e-j} \mathbf{U}^{e-j} + \underline{\boldsymbol{\mathcal{K}}}^{e+j} \mathbf{U}^{e+j}\right),$$

where $\mathbf{U}^e = [U_0^e, \ldots, U_p^e]$ is the vector of unknown DOFs and $\underline{\boldsymbol{\mathcal{L}}}, \underline{\boldsymbol{\mathcal{K}}}$ are constant matrices. These matrices depend on the considered scheme. For compact schemes such as the **BR2/SIPG** and **LDG** in 1D, $N_{nbe} = 1$, while for the **BR1** method, $N_{nbe} = 2$. This results in a system of $p + 1$ semidiscrete equations for the unknown DOFs.

2.3.1. A stabilized BR1. The original **BR1** method [5] was reported to be weakly unstable in general; see [6, 7, 3, 23]. Therefore, motivated by the work of Kannan and Wang [25], we introduce a modified/stabilized version of the **BR1** method, in which $\hat{\Theta}$ is defined as

$$(2.14) \qquad \hat{\Theta} = \{\!\{\Theta^e\}\!\} - \alpha^{br1}(\llbracket u \rrbracket), \qquad \alpha^{br1}(\llbracket u \rrbracket) = -\eta_f^{br1} \frac{C(p)}{h_e} \llbracket u \rrbracket,$$

where $\eta_f^{br1} \geq 0$ and $C(p) = (p+1)^2/2$. By substituting $\hat{u}$ from Table 1 in (2.7), we can define the auxiliary variable Θ^e as

$$(2.15) \qquad \Theta^e = \frac{\partial u^e}{\partial x} + R^e\left(\llbracket u \rrbracket\right),$$

where $R^e\left(\llbracket u \rrbracket\right)$ is a global lifting operator defined as

$$(2.16) \qquad \int_{\Omega_e} R^e\left(\llbracket u \rrbracket\right) \phi \, \mathrm{d}x = \int_{\partial \Omega_e} \left(\hat{u} - u^e\right) \phi \cdot \boldsymbol{n} \, \mathrm{d}s = -\frac{1}{2} \sum_{f \in \partial \Omega_e} \llbracket u \rrbracket\big|_f \, \phi\big|_f.$$

We note the jumps at interfaces of Ω_e using $\hat{u}$ of the **BR1**:

$$(2.17) \qquad \left(\hat{u} - u^e\right)\big|_{e-1/2} = \frac{1}{2}\llbracket u \rrbracket\big|_{e-1/2}, \qquad \left(\hat{u} - u^e\right)\big|_{e+1/2} = -\frac{1}{2}\llbracket u \rrbracket\big|_{e+1/2}.$$

The choice of the form of $\alpha^{br1}(\llbracket u \rrbracket)$ is also motivated by the result of Lemma C.2 in Appendix C for computing $\{\!\{R^e(\llbracket u \rrbracket)\}\!\}$,

$$(2.18) \qquad \{\!\{R^e(\llbracket u \rrbracket)\}\!\}_{e\pm1/2} = -\frac{C(p)}{h}\llbracket u \rrbracket_{e\pm1/2} + \frac{C1(p)}{h}\left(\llbracket u \rrbracket_{e\pm3/2} + \llbracket u \rrbracket_{e\mp1/2}\right),$$

where $C(p) = (p+1)^2/2$, $C1(p) = (-1)^{p+1}(p+1)/4$. In addition, we will see later in this work that the first term on the right-hand side of (2.18) is similar to the penalty term for the **SIPG** and **BR2** methods.

The only difference between the **BR1** and **BR2** methods is related to the additional terms on the right-hand side of (2.18), which are responsible for the noncompactness of this scheme. This is because these additional terms do not only depend on the immediate neighbors of Ω_e, namely, Ω_{e-1}, Ω_{e+1}, but also on their neighbors, i.e., Ω_{e-2}, Ω_{e+2}. In the rest of the paper we adopt this stabilized form of **BR1**, as it encompasses the original one.

2.3.2. SIPG and BR2. In the original **BR2** method [6], $\alpha^{br2}(\llbracket u \rrbracket)$ was defined as

$$(2.19) \qquad \alpha^{br2}(\llbracket u \rrbracket) = -\{\!\{r_f(\llbracket u \rrbracket)\}\!\},$$

where the local lifting operator r_f can be computed in 1D from

$$(2.20) \qquad \int_{\Omega_e} r_f(\llbracket u \rrbracket) \phi \, \mathrm{d}x = \int_f \left(\hat{u} - u^e\right) \phi \cdot \boldsymbol{n} \, \mathrm{d}s = -\frac{1}{2}\llbracket u \rrbracket\big|_f \, \phi\big|_f.$$

Note that the jumps at interfaces of Ω_e are computed in the same way as in (2.17). Brezzi et al. [7] have shown that to ensure the coercivity of the bilinear form, a penalty parameter $\eta_f^{br2} \geq N_f$ has to be included such that

$$(2.21) \qquad \alpha^{br2}(\llbracket u \rrbracket) = -\eta_f^{br2}\{\!\{r_f(\llbracket u \rrbracket)\}\!\},$$

where N_f is the number of faces of an element. It can be shown that this definition of $\alpha^{br2}(\llbracket u \rrbracket)$ reduces to the one in (2.12) under some conditions in 1D. In particular, we can establish equivalence between the **SIPG** and **BR2** methods by taking $C(\mathrm{p}) = (\mathrm{p}+1)^2/2$ as was suggested by [40, 23] and proved mathematically by Quaegebeur et al. [31] in the ESFR framework. For the sake of completeness, we also show their equivalence in the DG framework in Appendix B.

2.3.3. LDG. The **LDG** formulation was proposed in [10] as a generalization for the **BR1** method. The parameter $\beta_f \in \mathbb{R}$ is a scalar value in 1D, possibly face-dependent. For a compact **LDG** scheme in 1D, $\beta_f \in \{-\frac{1}{2}, \frac{1}{2}\}$; see [10, 30]. Using the definition of the **LDG** numerical flux $\hat{u}$ from Table 1 in (2.7), we can see that Θ^e for this method reads as

$$(2.22) \qquad \Theta^e = \frac{\partial u^e}{\partial x} + R^e\big(\beta[\![u]\!]\big),$$

where for Ω_e, in 1D,

$$(2.23) \quad \int_{\Omega_e} R^e\big(\beta[\![u]\!]\big)\phi\,\mathrm{d}x = \int_{\partial\Omega_e} (\hat{u} - u^e)\,\phi\cdot\boldsymbol{n}\,\mathrm{d}s = -\sum_{f\in\partial\Omega_e} \left(\frac{1}{2} + \beta_f\right) [\![u]\!]\big|_f\,\phi\big|_f.$$

For a certain face f, if we choose $\beta_f = \frac{1}{2}$, we get

$$(2.24) \qquad \hat{u} = u^+,$$

$$(2.25) \qquad \hat{\Theta} = \Theta^- - \frac{\eta_f^{ldg}}{h_e}[\![u]\!],$$

where we have chosen $C(\mathrm{p}) = 1$ in this case. Note that in 1D, this schemes is compact due to the fact that if $(\beta_f = 1/2)$ for the right face of Ω_e, it will be $(\beta_f = -1/2)$ for the other one, and hence (2.23) will have support on one face only. In this regard, it is similar to the CDG method in 1D but becomes noncompact in 2D.

2.3.4. CDG. The **CDG** [30] method is a compact extension of the **LDG** in multiple dimensions. It preserves the good properties of the **LDG** while eliminating the problem of noncompactness and sensitivity to the switch $\boldsymbol{\beta}_f$ as indicated in [30]. In this method, we use an edge-based $\boldsymbol{\Theta}_f^e$ in the numerical fluxes defined as

$$(2.26) \qquad \boldsymbol{\Theta}_f^e = \nabla u^e + \boldsymbol{r}^e\left(\beta[\![u^e]\!]\right),$$

where

$$(2.27) \qquad \boldsymbol{r}^e\left(\beta[\![u^e]\!]\right) = -\int_f \left(\frac{1}{2} + \boldsymbol{\beta}_f\cdot\boldsymbol{n}\right) [\![u^e]\!]\cdot\phi\boldsymbol{n}\,\mathrm{d}s.$$

This form of the edge-based $\boldsymbol{\Theta}_f^e$ results in a compact scheme where $\boldsymbol{r}^e\left(\beta[\![u^e]\!]\right)$ is a polynomial for each edge similar to $r_f^e\left([\![u^e]\!]\right)$ of the **BR2**. In 2D, $\boldsymbol{\beta}_f$ is a vector given by

$$(2.28) \qquad \boldsymbol{\beta}_f = \frac{1}{2}\left(s_-^+\boldsymbol{n}^- + s_+^-\boldsymbol{n}^+\right),$$

where $s_-^+ \in \{0, 1\}$ is a switch defined for each face; i.e., s_-^+ denotes the switch for element Ω^- associated with the face shared by Ω_e^-, Ω_e^+. The switches always satisfy

$$(2.29) \qquad s_-^+ + s_+^- = 1$$

but are otherwise arbitrary as indicated in [30].

3. Semidiscrete Fourier analysis. Assuming a wavelike initial solution of the form

$$u(x,0) = u_o(x) = \exp(ikx) \tag{3.1}$$

for (2.1) results in the exact solution

$$u(x,t) = \exp(ikx - \omega t), \tag{3.2}$$

where k is the spatial wavenumber and ω denotes the frequency that admits an exact diffusion relation $\omega = \gamma k^2$. In a temporal semidiscrete Fourier analysis [38], a prescribed wavenumber k is assumed for the initial condition equation (3.1), and different spatial schemes are applied to (2.1) in order to study their diffusion properties based on a numerical frequency $\tilde{\omega}$.

The method used in this section for DG is similar to the one previously presented in [22, 29, 2] for the linear advection equation and Zhang and Yan [43] and Guo, Zhong, and Qiu [19] for the linear heat equation, among others. For the DG method, the elementwise DOFs U_j^e are related to the wave solution equation (3.2) through L_2 projection onto the solution basis. Therefore, for the initial wave solution equation (3.1), the elementwise DOFs U_l^e can be computed as

$$U_l^e(0) = \frac{\int_{\Omega_e} u^e(x,0)\,\phi_l(x)\,\mathrm{d}x}{\int_{\Omega_e} \phi_l(x)\,\phi_l(x)\,\mathrm{d}x} = \frac{\int_{\Omega_s} u(x_e + \xi\,h/2, 0)\,\phi_l(\xi)\,\mathrm{d}\xi}{M_{ll}} = \hat{\mu}_l\,\exp(ikx_e), \tag{3.3}$$

where

$$\hat{\mu}_l = \frac{\int_{-1}^{1} \exp(ik\,(\xi h/2))\,\phi_l(\xi)d\xi}{M_{ll}}. \tag{3.4}$$

It is easy to see that the exact DG solution for the DOFs can be expressed as

$$U_l^e(t) = \mu_l\exp(ikx_e - \omega t), \tag{3.5}$$

where $\mu_l = \hat{\mu}_l$ for the exact solution. Seeking a similar solution to (3.5) and substituting into (2.13) results in

$$\left(\frac{h_e^2}{\gamma}\right)\frac{\partial \mathbf{U}^e}{\partial t} = \left[\underline{\boldsymbol{\mathcal{L}}} + \sum_{j=1}^{N_{nbe}}\left(\underline{\boldsymbol{\mathcal{K}}}^{e-j}\exp(-j(ikh)) + \underline{\boldsymbol{\mathcal{K}}}^{e+j}\exp(j(ikh))\right)\right]\mathbf{U}^e. \tag{3.6}$$

By differentiating (3.6), we get the semidiscrete relation

$$\lambda\,\boldsymbol{\mu} = \underline{\boldsymbol{\mathcal{A}}}\,\boldsymbol{\mu}, \qquad \lambda = -\left(\frac{h^2}{\gamma}\tilde{\omega}\right). \tag{3.7}$$

Assuming a real wavenumber k and a numerical frequency $\tilde{\omega}$, the semidiscrete system equation (3.7) constitutes an eigenvalue problem with $p+1$ eigenpairs, $(\lambda_j, \boldsymbol{\mu}_j)$, $j = 0, \ldots, p$, for the semidiscrete matrix $\underline{\boldsymbol{\mathcal{A}}}$. For this type of system, all the eigenvalues of the matrix $\underline{\boldsymbol{\mathcal{A}}}$ are real for all schemes under consideration. The general solution equation (3.5) can be written as a linear expansion in the eigenvectors space

$$\mathbf{U}^e(t) = \sum_{j=0}^{p} \vartheta_j\,\boldsymbol{\mu}_j\,\exp(ikx_e - \tilde{\omega}_j t). \tag{3.8}$$

The expansion coefficients ϑ_j are obtained by satisfying the initial condition equation (3.1) for $t = 0$. As a result, these coefficients are given by

$$(3.9) \qquad \hat{\boldsymbol{\mu}} = \sum_{j=0}^{p} \vartheta_j \, \boldsymbol{\mu}_j \quad \text{or} \quad \boldsymbol{\vartheta} = \underline{\boldsymbol{\mathcal{M}}}^{-1} \, \hat{\boldsymbol{\mu}},$$

where $\underline{\boldsymbol{\mathcal{M}}} = \left[\boldsymbol{\mu}_0, \ldots, \boldsymbol{\mu}_p \right]$ is the matrix of eigenvectors and $\boldsymbol{\vartheta} = [\vartheta_0, \ldots, \vartheta_p]^T$. The numerical solution can now be computed using (2.9) with the DOFs given by (3.8) to yield

$$(3.10) \qquad u^e(\xi, t) = \sum_{l=0}^{p} \sum_{j=0}^{p} \vartheta_j \mathcal{M}_{l,j} \, \exp\left(ikx_e - \tilde{\omega}_j t\right) \phi_l(\xi),$$

while the exact solution can be written as

$$(3.11) \qquad u_{ex}^e(\xi, t) = \sum_{l=0}^{p} \hat{\mu}_l \, \exp\left(ikx_e - \omega t\right) \phi_l(\xi).$$

The numerical solution (3.10) is essentially a linear combination of $p + 1$ eigenmodes. Each eigenmode has its own numerical diffusion behavior. In order to assess the numerical dissipation of a DG scheme based on a certain eigenmode, we define the nondimensional wavenumber as

$$(3.12) \qquad K = \frac{kh}{p+1}, \quad 0 \le kh \le (p+1)\pi.$$

Similarly, by defining the modified/numerical wavenumber $k_m^2 = \tilde{\omega}/\gamma$, we can obtain a similar expression for the nondimensional wavenumber K_m. Note that $h/(p+1)$ is a measure of the smallest length-scale that can be captured by a DG scheme [29, 2]. The numerical scheme induces numerical dissipation through $\mathcal{R}e(\tilde{\omega})$, whereas numerical dispersion for all schemes studied in this work is zero since $\tilde{\omega}$ is always real. In this case, the numerical diffusion relation reads as

$$(3.13) \qquad \mathcal{R}e\left((\tilde{\omega}/\gamma)\, h^2\right) = \mathcal{R}e((k_m\, h)^2) \approx (k\, h)^2.$$

3.1. Eigenmode approach. In this section, we discuss the Fourier analysis results based on the individual modes as it is usually performed for the linear heat equation [23, 25]. We start by defining a relative weight measure [4] among eigenmodes in order to quantify the contribution of each mode to the total solution along the extended wavenumber range. This relative weight measure is defined based on the weights $\boldsymbol{\vartheta}$ of the normalized eigenvectors

$$(3.14) \qquad \Gamma_l = |\vartheta_l|^2 / \sum_{j=0}^{p} |\vartheta_j|^2, \quad l = 0, \ldots, p,$$

where Γ_l is the relative weight of eigenmode l.

Figure 1 presents the eigenmode dissipation curves as well as the relative weight distribution curves for the **BR2**p2-η1 scheme as an example. Note that in the rest of this paper we drop the subscript f from η_f, so that $\eta = \eta_f$, constant for all faces. In addition, if a particular order p and η parameter are specified, we use the notation **BR1**p2-η0, **BR2**p2-η1, and **LDG**p2-η0 as examples for p2 spatial DG schemes.
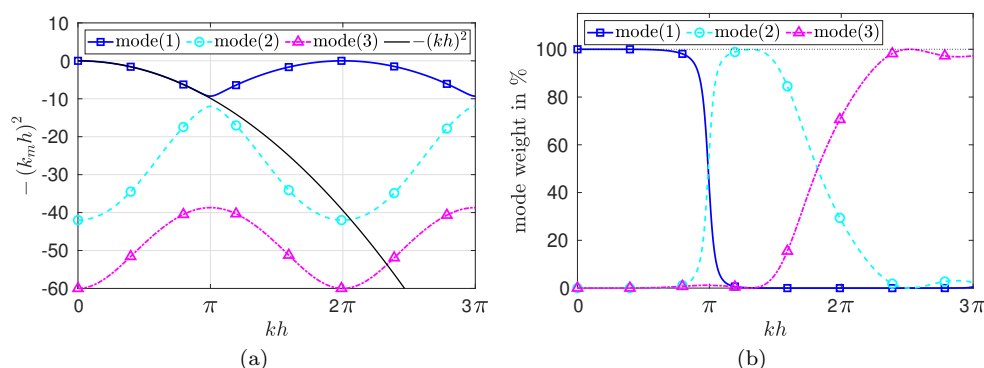
FIG. 1. *Semidiscrete dissipation (left) based on individual eigenvalues and eigenmode relative energy curves (right) for the BRp2-η1 scheme. In this figure, mode(1) is identified as the physical-mode.*

For multi-DOF high-order methods, the wavenumber range of the initial Fourier mode can be extended up to $kh \leq (p+1)\pi$ due to their local number of degrees of freedom (nDOFs) of $(p+1)$ in each element. Therefore, it is expected that these schemes should approximate the exact diffusion for a wider range of the extended wavenumber. However, by inspecting Figure 1(a), we can see that mode(1), or the so-called *physical-mode* [22], only approximates the exact diffusion up to $kh \approx \pi$. Indeed, mode(1) has the largest relative weight up to $kh \approx \pi$ according to Figure 1(b). For $kh > \pi$, we can see that the other two modes alternate in sharing the highest relative weight, and near $kh \approx 2\pi$, both share equal weights of $\approx 50\%$. This suggests that the *physical-mode* choice should be changed to mode(2) and then to mode(3) as we approach $kh = 3\pi$. In addition, it can also be concluded that the coupling between eigenmodes is very important, and they all cooperate to approximate the exact diffusion relation for the entire range of wavenumbers. This problem of the coupling between eigenmodes and the failure of the *physical-mode* to approximate the exact diffusion as expected was not carefully addressed in the literature [23, 25]. Therefore, we propose the *combined-mode* analysis as a new approach to overcome these shortcomings of the classical analysis. For the other two formulations (**BR1, LDG**), the general trend is the same as the example presented in this section.

3.1.1. von Neumann stability analysis. In order to facilitate the study of the penalty parameter influence on the diffusion behavior of the considered schemes, we first compute the range of penalty parameters to ensure the von Neumann stability. The von Neumann stability condition of a certain scheme ensures the solution does not grow in time. This condition is satisfied if for all eigenmodes, $-(k_m h)^2 \leq 0$. Note that this condition is equivalent to $\lambda \leq 0$. In studying the stability of a certain scheme we assume a range of prescribed wavenumbers $kh \in [0, (p+1)\pi]$, and for a certain value of η we check the sign of λ for all eigenmodes. If $\lambda > 0$, this means the scheme has a growing mode and hence is unstable.

Since the penalty term is necessary for the stability of a **BR2** scheme [3], we choose a range of $\eta^{br2} \in (0, 3]$, while for **LDG** schemes we tried both negative and positive values for η^{ldg}. It turned out that the **LDG** scheme is indeed stable for negative η values, unlike the **BR2**, which has a minimum positive value. Tables 2 and 3 present the stability analysis results for **BR2** and **LDG**, respectively. From these tables, we can conclude that the minimum η for the stabilization

TABLE 2
*Minimum magnitude of penalty η for a stable DG scheme with **BR2**.*

p	1	2	3	4	5	6	7	8
η	0.50	0.67	0.75	0.80	0.83	0.86	0.88	0.89

TABLE 3
*Minimum magnitude of penalty η for a stable **LDG** scheme.*

p	1	2	3	4	5	6	7	8
η	-3	-5	-7	-9	-11	-13	-15	-17

of **BR2** schemes has the relation

$$(3.15a) \qquad \min\left(\eta^{br2}\right) = \frac{p}{p+1}, \quad \lim_{p \to \infty} \min\left(\eta^{br2}\right) = 1.0, \quad p \geq 1,$$

while for the **LDG**

$$(3.15b) \qquad \min\left(\eta^{ldg}\right) = -\left(2p+1\right), \quad p \geq 1.$$

On the other hand, the stabilized **BR1** schemes have a minimum $\eta^{br1} = 0$ for all orders. These results has been verified numerically as well. The optimal choice for η obviously depends on a number of factors concerning the accuracy, stability, and robustness of a diffusion scheme. This is investigated in more detail in the rest of this paper. We note that von Neumann stability is a necessary and sufficient condition for the stability of a Cauchy problem.[1] For more general problems this condition is not sufficient.

3.2. Combined-mode approach. The *combined-mode* analysis was first introduced in [2] to study the *true* dispersion-dissipation behavior of DG and Runge–Kutta DG (RKDG) schemes for linear advection. In this approach all eigenmodes resulting from Fourier analysis are considered in computing the response of the semidiscrete system for an initial wave mode of the form in (3.1). We extend the *combined-mode* analysis to DG schemes for diffusion using the linear heat equation. In this regard, it is convenient to define two nondimensional timescales as

$$(3.16) \qquad \tau = \frac{\gamma t}{h^2}, \qquad \tau_p = (p+1)^2 \tau,$$

where τ, τ_p are the nondimensional diffusion timescales based on the cell width h and the smallest length-scale of a DG scheme $h/(p+1)$, respectively. The timescale τ represents the diffusion timescale for single DOF methods through an area h^2. The second timescale τ_p represents the time required for the diffusion of a wave per DOF of a DG scheme through an area $(h/p+1)^2$.

---

[1] The Cauchy problem in this article is the IBVP in an infinite domain$(-\infty, \infty)$, i.e., (2.1) with periodic boundary conditions.

In this approach, the wave energy on Ω_s using the L_2 norm of a complex function at any time τ_p is given by

$$
\begin{aligned}
E(k, \tau_p) &= \left(\frac{1}{h_e} \int_{\Omega_e} \left| u^e(\xi, \tau_p) \right|^2 \, \mathrm{d}x \right)^{1/2} \\
&= \left(\frac{1}{h_e} \int_{-1}^{1} \left| u^e(\xi, \tau_p) \right|^2 \frac{h_e}{2} \, \mathrm{d}\xi \right)^{1/2} \\
&= \left(\frac{1}{2} \int_{-1}^{1} \left| \sum_{l=0}^{p} U_l \phi_l(\xi) \right|^2 \, \mathrm{d}\xi \right)^{1/2} \\
&= \left(\frac{1}{2} \int_{-1}^{1} \left| \sum_{l=0}^{p} \sum_{j=0}^{p} \vartheta_j \mathcal{M}_{l,j} \, \exp\left(-K_{m,j}^2 \tau_p \right) \phi_l(\xi) \right|^2 \, \mathrm{d}\xi \right)^{1/2},
\end{aligned}
\tag{3.17}
$$

while the exact energy is defined as

$$
\begin{aligned}
E_{ex}(k, \tau_p) &= \left(\frac{1}{2} \int_{-1}^{1} \left| u_{ex}^e(\xi, \tau_p) \right|^2 \, \mathrm{d}\xi \right)^{1/2}, \\
&= \left(\frac{1}{2} \int_{-1}^{1} \left| \sum_{l=0}^{p} \hat{\mu}_l \, \exp\left(-K^2 \tau_p \right) \phi_l(\xi) \right|^2 \, \mathrm{d}\xi \right)^{1/2},
\end{aligned}
\tag{3.18}
$$

where we have eliminated $\exp(ikx_e)$ since it does not affect the above equations. This definition of the energy is equivalent to an averaged amplitude over Ω_e. The *combined-mode* analysis defines the *true* diffusion factor as

$$
G_{true}(k, \tau_p) = \frac{E(k, \tau_p)}{E_{ex}(k, 0)} = \frac{E^e(k, \tau_p)}{E_{initial}^e(k)},
\tag{3.19}
$$

while the *physical-mode* diffusion factor is given by

$$
G_{phys}(k, \tau_p) = \exp\left(-\tilde{\omega}\, t \right) = \exp\left(-K_m^2 \, \tau_p \right).
\tag{3.20}
$$

In addition, the diffusion behavior can be further assessed in the low wavenumber range ($K < \pi/2$) by computing the diffusion error, defined as the relative absolute difference between the numerical and exact diffusion factors

$$
\left| \frac{G_{ex} - G}{G_{ex}} \right| = \left| 1 - \frac{G}{G_{ex}} \right| = \left| 1 - \rho \right|,
\tag{3.21}
$$

where ρ is the ratio of the numerical diffusion factor to the exact one and $G_{ex} = \exp(-K^2 \tau_p)$.

In summary, the *combined-mode* approach introduces a new definition for the diffusion factor that takes into account the contribution of all eigenmodes resulting from the classical Fourier analysis technique. In this way, there is no need to distinguish physical and parasite/spurious modes, as all of them are important for the accuracy of a DG scheme for diffusion, i.e., in approximating the exact diffusion.

Figure 2 presents the results of the semidiscrete *combined-mode* analysis in comparison to the standard Fourier analysis (based on the physical-mode) for the **LDG**p2-η0 scheme as an example. In Figure 2(a), it can be seen clearly that the *physical-mode*
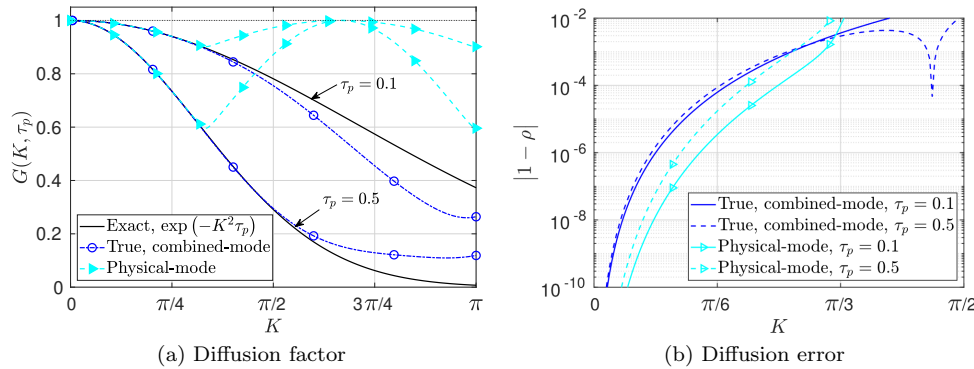
FIG. 2. *Semidiscrete diffusion analysis of the LDGp2-η0. Comparison of true and physical-mode behaviors.*

approximates the exact dissipation for only a small range of wavenumbers $K \leq \pi/3$. The *true* behavior, as a result of the *combined-mode* analysis, is sufficiently accurate in comparison with the exact one for a wider range of wavenumbers (up to $K = \pi$). In addition, by computing the diffusion errors equation (3.21), we can see in Figure 2(b) that the *physical-mode* underestimates the diffusion error in comparison to the *combined mode*. The difference between the diffusion error of the *combined mode* and that of the *physical-mode* is more than an order of magnitude for short time simulations ($\tau_p = 0.1$). This indicates that for a very low wavenumber range, the *physical-mode* cannot provide an accurate representation of the diffusion error without including the contribution of all the eigenmodes for up to $\tau_p = 0.5$. We want to emphasize that as τ_p becomes larger, the physical-mode behavior approaches the *combined-mode* behavior in the low wavenumber range. This is related to the decaying rate of the secondary modes in the low wavenumber range, as Guo, Zhong, and Qiu [19] have shown symbolically.

For long time simulations, $\tau_p = 0.5$ in Figure 2(a), the *true* behavior shows that less than exact dissipation can occur for high wavenumbers. While still stable, this high wavenumber behavior could trigger some aliasing and stability issues for nonlinear problems. It is always desirable to have more dissipation for high wavenumbers than the exact dissipation in underresolved large eddy simulations (LES). Figure 2 indicates the effectiveness of the *combined-mode* analysis for studying the *true* diffusion behavior of DG schemes for diffusion.

3.2.1. Diffusion characteristics and the influence of the penalty parameter and polynomial orders. In this section, we distinguish between short and long time diffusion behaviors. The classical eigenmode analysis suggests that the individual eigenvalue dissipation characteristics with respect to the exact dissipation remains the same for long time; i.e., long time is just an accumulation of more errors. This is because from a dynamical system point of view, that system with a single DOF has only one exponential decaying function with exponent that is a constant multiple of time. In contrast, for multi-DOF dynamical systems the behavior is highly nonlinear in time, and the interaction between the eigenmodes controls the behavior of the system. Moreover, through *combined-mode* analysis one can see that the combination of all modes results in a very different behavior for short and long time simulations.
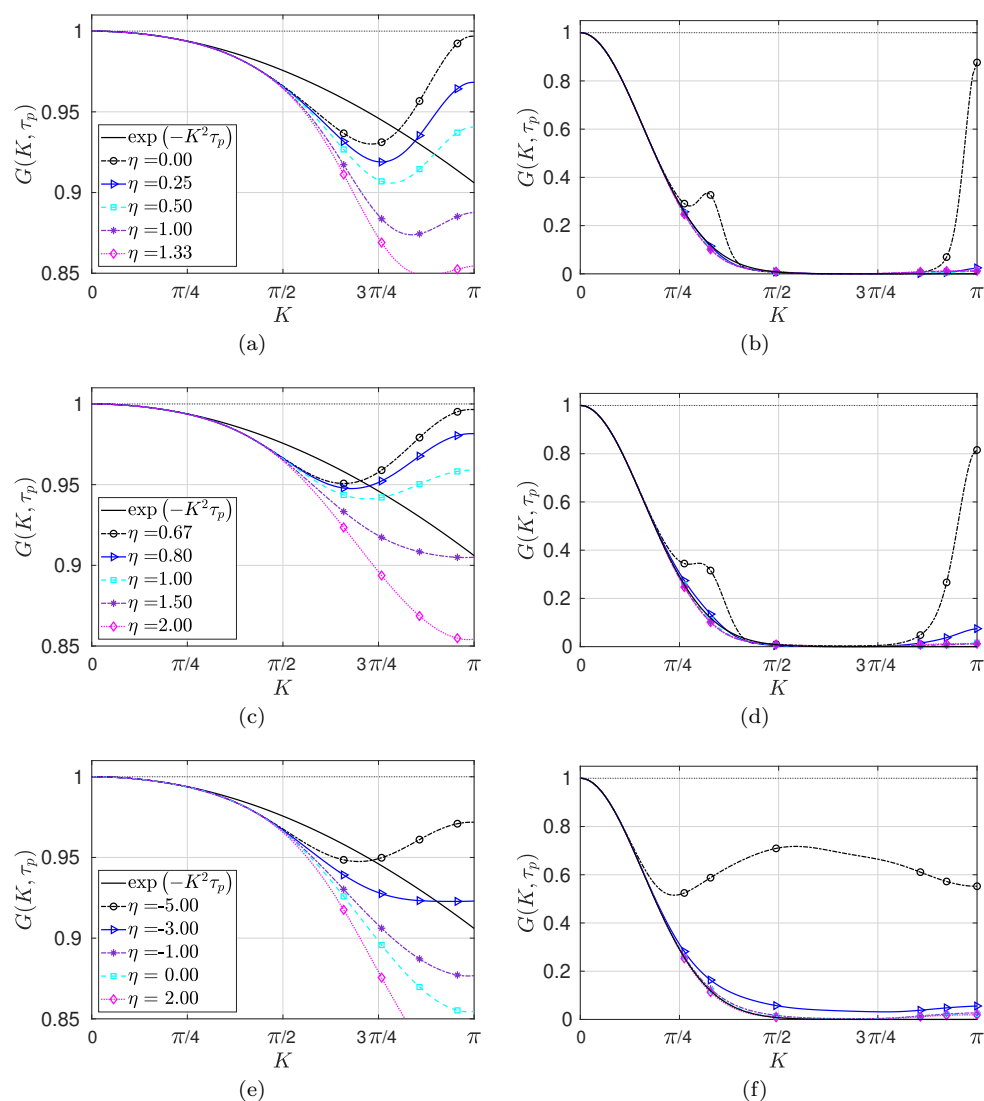
Fig. 3. *Effect of the penalty parameter on the semidiscrete diffusion of p2 schemes for short time $\tau_p = 0.01$ (left) and long time $\tau_p = 2.0$ (right) simulations. From top to bottom we have* **BR1**, **BR2**, *and* **LDG**.

We start by studying the effects of the penalty parameter η on the diffusion behavior of the **BR1**, **BR2**, and **LDG** formulations. Figure 3 presents the short and long time diffusion factors as a function of η. From this figure, as η increases, all schemes have a general trend of increasing the dissipation for high wavenumbers. The long time diffusion behavior is presented in the right column of Figure 3, where we can see that for very low values of η or minimum values for stability, the scheme becomes non robust due to very low and less than exact diffusion for high wavenumbers ($K \gtrsim 3\pi/4$). We can also notice some regions of saturation of the diffusion factor where the decaying rate becomes so slow in long time simulations. Moreover, by inspecting Figure 4, we can see that increasing η increases the diffusion error in the low wavenumber range ($K \leq \pi/2$) for all schemes.
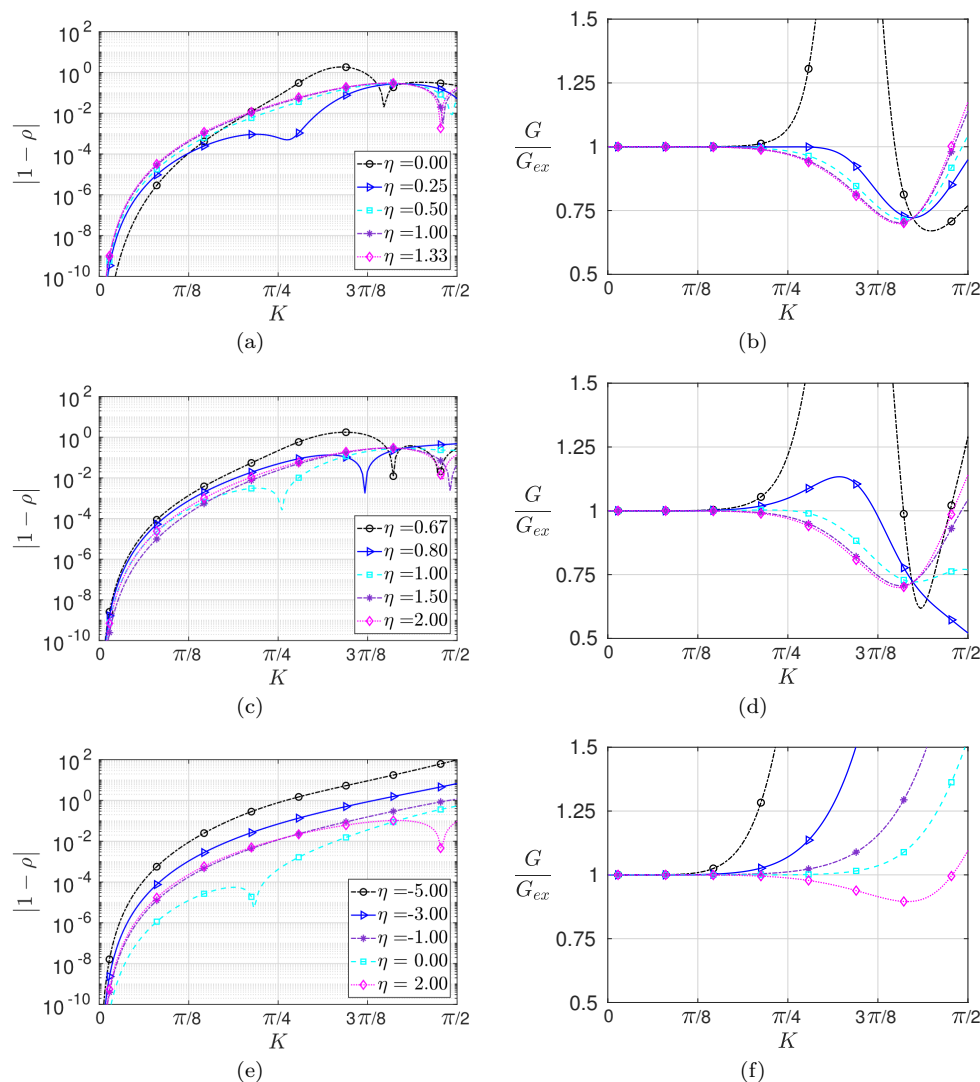
FIG. 4. *Effect of the penalty parameter on the semidiscrete diffusion errors in the low wavenumber range for long time simulations $\tau_p = 2.0$. From top to bottom we have* **BR1**, **BR2**, *and* **LDG**. *On the left are diffusion errors, while on the right are diffusion factor ratios.*

For the **BR2**p2 schemes, it can be seen from Figures 3(c) and 3(d) that an $\eta \geq 1.5$ provides larger than exact dissipation for $K \gtrsim 3\pi/4$ without sacrificing the low wavenumber accuracy and hence is beneficial for robust simulations. This can also be noticed by inspecting the diffusion factors ratios in Figure 4(d). In addition, for the **BR1**p2-η0, the diffusion factor at the Nyquist frequency $K = \pi$ has a very slow decaying rate that almost saturates at some value for a long time of the simulation. This behavior is similar to the case of RKDG schemes for advection with central fluxes [2], where it was reported that the amplification factor of the scheme saturates at some level for a very large number of iterations at $K = \pi$. It is mainly attributed to having a zero eigenvalue dissipation coefficient at $K = \pi$ for one of the eigenmodes of the **BR1**p2-η0 (not shown).
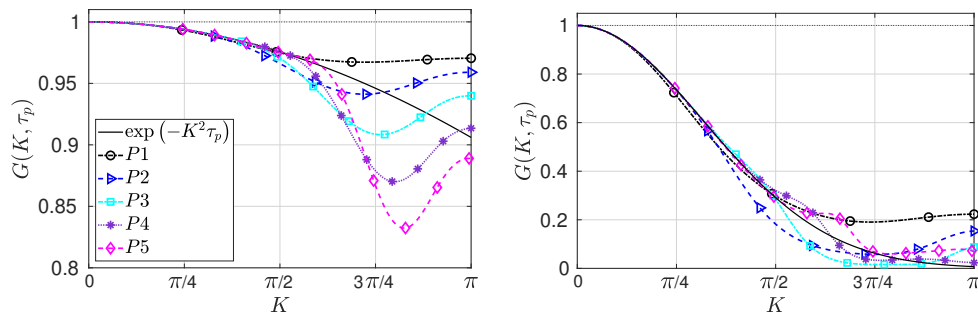
FIG. 5. *Effect of the polynomial order on the semidiscrete diffusion factor of* **BR2**-$\eta1$ *for short time simulations* $\tau_p = 0.01$ *(left) and relatively long time simulations* $\tau_p = 0.5$ *(right).*

The **LDG**p2-$\eta0$ scheme in its standard form is better than all the stabilized **LDG**p2 schemes with different η in terms of accuracy and robustness. For long time simulations, we can see in Figure 4(e) that this scheme has the least diffusion errors for low wavenumbers ($K \leq 3\pi/8$) among all the other **LDG** schemes with nonzero η values. Moreover, from Figure 3(e) it is clear that, for short time simulations, this scheme is more dissipative than the exact solution for moderate to high wavenumbers $K > \pi/2$.

If we carefully investigate the diffusion errors based on the both $|1 - \rho|$ and $\rho = G/G_{ex}$ in Figure 4, we can find η that yields the most accurate and robust candidate in the low wavenumber range. For the **BR1** and **BR2** p2 schemes, the most accurate candidates are $\eta = 0.25$ and $\eta = 1$, respectively. These two schemes also possess less than exact dissipation for $\pi/4 \leq K \leq \pi/2$, while the most accurate candidate of the **LDG** formulation, the $\eta = 0$ scheme, possesses larger than exact dissipation. This particular scheme **LDG**-$\eta0$ has been shown to have larger than exact dissipation for short time simulations; see Figure 3(e). Indeed, short and long time behaviors are completely different, especially for moderate to high wavenumbers.

Next, we discuss the influence of the polynomial order on the *combined-mode* diffusion behavior of the considered schemes. We choose the **BR2** formulation as an example. Figure 5 shows the diffusion factor of **BR2**-$\eta1$ with p1–p5 polynomial orders. In general, as the order increases, the scheme becomes more accurate in the low wavenumber range and more dissipative for high wavenumbers. The **BR2**-$\eta1$ have less than exact dissipation for high wavenumbers. We can also notice that the behavior for high wavenumbers in short and long time simulations is again different. Similar observations hold for the **BR1** and **LDG** with minor differences.

3.2.2. Comparison of the diffusion characteristics for the considered schemes. The relative efficiencies between the three viscous flux approaches are further discussed by comparing the resolution of all schemes at the same τ_p. For the **BR1** and **BR2** approaches, we choose a penalty parameter that yields almost the same diffusion factor at the Nyquist frequency as the **LDG**-$\eta0$ when $\tau_p = 0.01$ (short time). This diffusion factor provides higher than the exact dissipation for $K \gtrsim \pi/2$. This way we include a possibly robust versions of these schemes.

In Figure 6, we present the comparisons for short and relatively long times, i.e., at $\tau_p = 0.01$, $\tau_p = 0.50$. From this figure it can be noticed that with careful tuning of η, we can achieve very similar behaviors between different schemes. According to Figure 6(a), the diffusion factor of **BR2**p2-$\eta2$ is very close to the **LDG**-$\eta0$ one. In
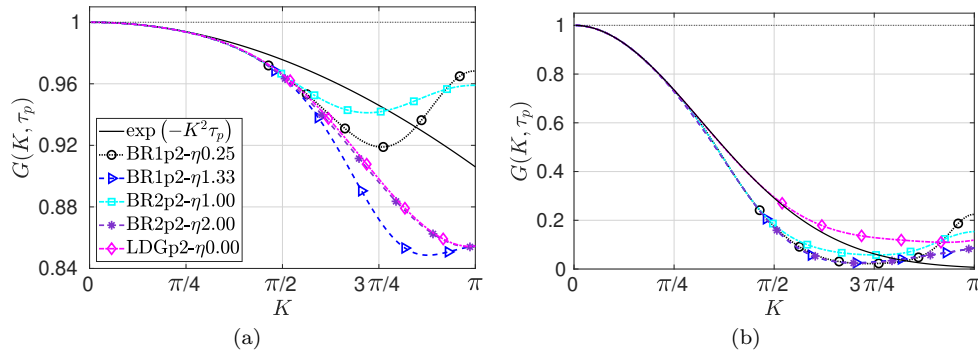
FIG. 6. *Comparison of the diffusion behavior of several p2 diffusion schemes for short time* $\tau_p = 0.01$ *(left) and relatively long time* $\tau_p = 0.5$ *(right) simulations.*
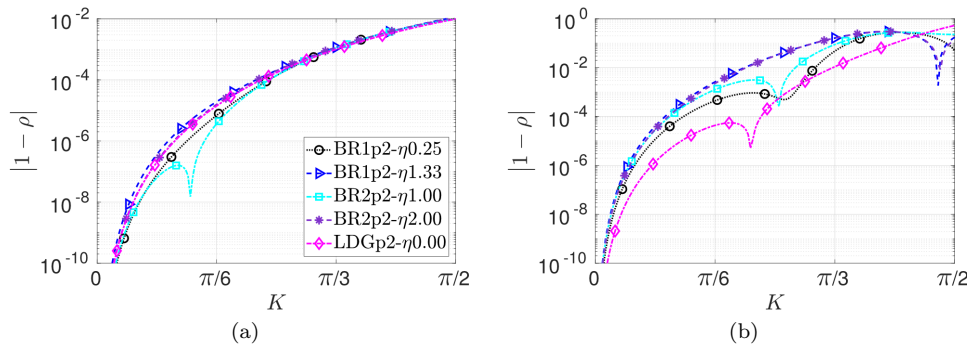

FIG. 7. *Comparison of the diffusion errors of p2 diffusion schemes for short time* $\tau_p = 0.01$ *(left) and long time* $\tau_p = 2.0$ *(right) simulations.*

addition, the diffusion factor of the **BR1**p2-η1.33 scheme is very close to that of the **BR2**p2-η2 scheme for both short and long time simulations. This can be understood in the context of similarities between them, as pointed out in subsection 2.3. However, it is worth noting that their behavior for $K > \pi/2$ is not exactly similar, possibly due to the noncompactness of **BR1** induced by the additional terms in (2.18).

We also note that matching the same amount of dissipation at the Nyquist frequency requires different η values for different orders; e.g., for p5 this can be achieved with $\eta^{br1} = 0.80$, $\eta^{br2} = 1.65$. This suggests that schemes with asymptotically similar diffusion factors can also be achieved for high orders. One particularly interesting scheme is **BR1**p2-η0.25, which serves as a good alternative for the standard **BR1**p2-η0 with even fewer low wavenumber errors than **BR1**p2-η1.33; Figure 7. Despite the similarities between these schemes, the standard **LDG** scheme maintained a better error bound than **BR1** and **BR2** schemes for low wavenumbers, $K \leq \pi/2$; see Figure 7 for long time simulations. We also note that although the **BR1**p2-η1 has shown slightly less diffusion error than the **LDG**p2-η0, $K \lesssim \pi/3$, for short time simulations in Figure 7(a), the situation changed completely for long time simulations.

3.2.3. Evolution of the diffusion error with time. In this section we study the evolution of the diffusion error with time for all schemes in the low wavenumber range $K \leq \pi/2$. Based on the results of the previous section, we choose two values for
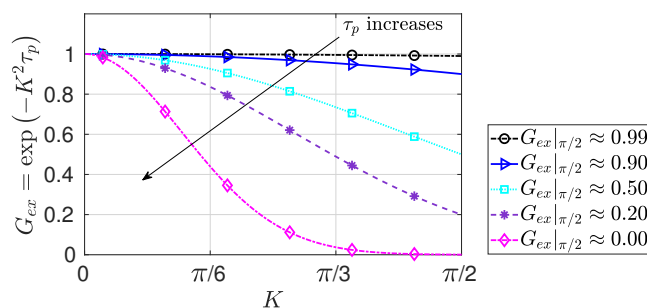
FIG. 8. *Evolution of the exact semidiscrete diffusion factor with time in the low wavenumber range $K \leq \pi/2$.*
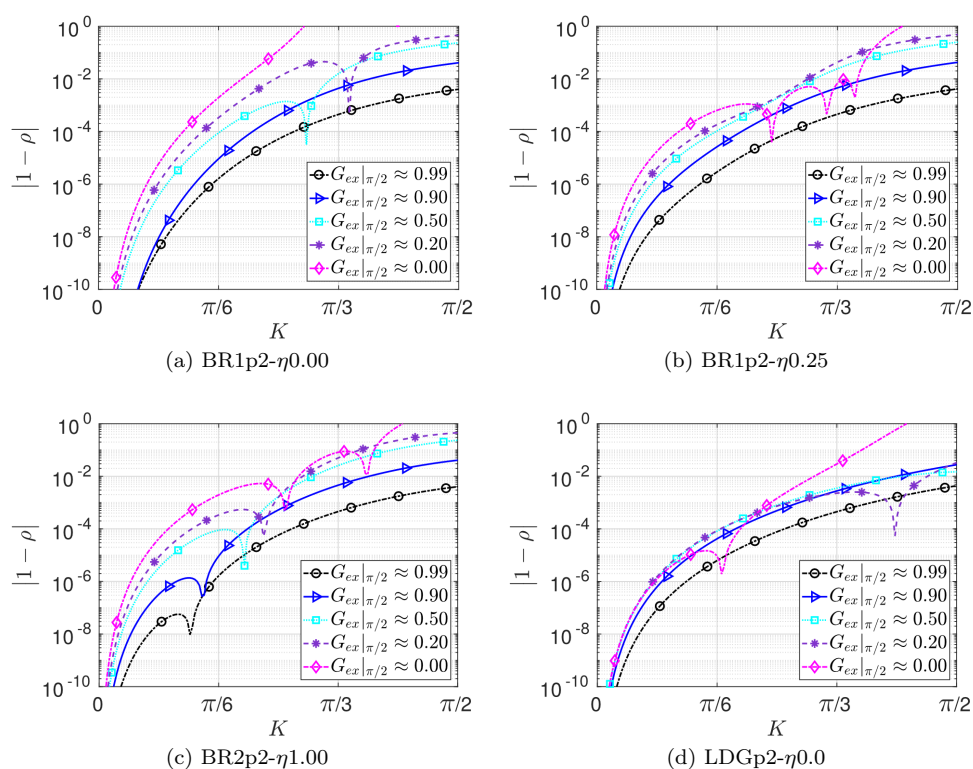

(a) BR1p2-η0.00

(b) BR1p2-η0.25

(c) BR2p2-η1.00

(d) LDGp2-η0.0

FIG. 9. *Evolution of the semidiscrete diffusion error with time for $p2$ spatial schemes.*

η, namely, $\eta^{br1} = 0.0$, $\eta^{br1} = 0.25$, for the **BR1**p2 scheme while using the standard form for the **BR2**p2 and **LDG**p2 schemes with minimum stabilization, i.e., $\eta^{br2} = 1, \eta^{ldg} = 0$. The error is computed at several instances in time where the exact diffusion factor G_{ex} of the initial Fourier mode at $K = \pi/2$ changes from $G_{ex}|_{\pi/2} \approx 0.99$ to $G_{ex}|_{\pi/2} \approx 0.00$; Figure 8. These values were chosen to highlight the importance of the resolution in the low wavenumber range for short and long time simulations.

The evolution of the error with time for a number of schemes is displayed in Figure 9. In this figure we can see that the **LDG**p2-η0 scheme maintains an upper bound on the error that is not exceeded as time evolves. The maximum error of this scheme
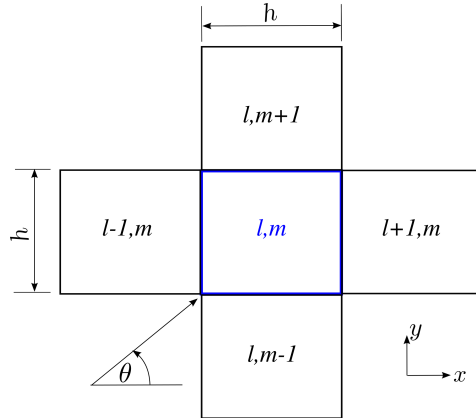
FIG. 10. *2D quadrilateral grid pattern.*

for $0 < K \lesssim \pi/4$ does not exceed $\approx 10^{-4}$, while for the **BR1**p2-η0, **BR1**p2-η0.25, and **BR2**p2-η1 schemes the error clearly exceeds this level. The diffusion errors for the **BR1**p2-η0, **BR1**p2-η0.25, and **BR2**p2-η1 schemes always increase faster than the **LDG**p2-η0 as time evolves.

3.3. Extension to 2D. In this section, we present, in brief, the extension of the *combined-mode* analysis for 2D meshes with quadrilateral elements, as shown in Figure 10. Following the 1D analysis, we assume an initial plane wave of the form

$$(3.22) \qquad u(x, y, 0) = \exp\left(ik(x\cos(\theta) + y\sin(\theta)\right),$$

where k is the wavenumber and $\theta \in [0, 2\pi]$ is the wave incidence angle measured from the positive x direction. For this type of grid, the DG method employs 2D basis formed by tensor products of the 1D basis in ξ, η directions, and this results in $nDOF = (p+1)^2$. The initial solution is projected onto the space of degree p polynomials in 2D, i.e., $[\mathcal{P}^p(\Omega_e)]^2$. This projection is defined as

$$(3.23) \qquad U_j^e(0) = \frac{\int_{\Omega_e} u(x,y,0)\,\phi_j(x,y)\,d\Omega_e}{\int_{\Omega_e} \phi_j(x,y)\,\phi_j(x,y)\,d\Omega_e} = \frac{\int_{\Omega_s} u(\xi,\eta,0)\,\phi_j(\xi,\eta)\,J\,d\Omega_s}{\int_{\Omega_s} \phi_j(\xi,\eta)\,\phi_j(\xi,\eta)\,J\,d\Omega_s},$$

where for the generating pattern in Figure 10 all the transformation metrics are constants. In particular, for an equal mesh size of $h_x = h_y = h$, the bilinear transformation is simplified to

$$(3.24) \qquad x(\xi) = x_e + (h/2)\xi, \quad y(\eta) = y_e + (h/2)\eta, \quad J = h^2/4.$$

The initial solution equation (3.22) can be written for the standard quadrilateral Ω_s in terms of computational coordinates (ξ, η) as

$$(3.25) \qquad u(\xi, \eta, 0) = \exp\left(ik\big[(x_e + (\xi h/2))\cos(\theta) + (y_e + (\eta h/2))\sin(\theta)\big]\right),$$

and by substituting (3.25) into (3.23) we get

$$(3.26) \qquad U_j^e(0) = \hat{\mu}_l^x\,\hat{\mu}_m^y\,\exp\left(ik\big[x_e\cos(\theta) + y_e\sin(\theta)\big]\right),$$

where $\hat{\mu}_l^x\,\hat{\mu}_m^y$ are defined as

(3.27)

$$\hat{\mu}_l^x = \frac{\int_{-1}^{1} \exp\left(ik\cos(\theta)(\xi h/2)\right)\phi_l(\xi)\,\mathrm{d}\xi}{M_{ll}}, \quad \hat{\mu}_m^y = \frac{\int_{-1}^{1} \exp\left(ik\sin(\theta)(\eta h/2)\right)\phi_m(\eta)\,\mathrm{d}\eta}{M_{mm}},$$

$$\phi_i(\xi,\eta) = \phi_l(\xi)\,\phi_m(\eta), \quad j = l(p+1)+m.$$

As a result, the exact DG solution can be expressed as

(3.28)
$$\mathbf{U}^e(t) = \boldsymbol{\mu}\,\exp\left(ik\big[x_e\cos(\theta) + y_e\sin(\theta)\big] - \omega t\right),$$

where $\boldsymbol{\mu} = \hat{\boldsymbol{\mu}} = [\hat{\mu}_0,\ldots,\hat{\mu}_N]^T$ and $\hat{\mu}_j = \hat{\mu}_l^x\hat{\mu}_m^y$, $N = (p+1)^2 - 1$. The semidiscrete equation for the 2D quadrilateral mesh in Figure 10 can be written as

(3.29)
$$\left(\frac{h_e^2}{\gamma}\right)\frac{\partial\mathbf{U}^{l,m}}{\partial t} = \left(\underline{\boldsymbol{\mathcal{L}}}\mathbf{U}^{l,m} + \sum_{e,j}\underline{\boldsymbol{\mathcal{K}}}^{e,j}\mathbf{U}^{e,j}\right),$$

where $(e,j) \in \{(l-1,m),(l+1,m),(l,m-1),(l,m+1))\}$ for a compact stencil of four neighbors. Note that in this section we only focus on compact schemes such as **BR2/SIPG** and **CDG** for efficiency and simplicity. Seeking a similar solution to (3.28) and substituting in (3.29) results in

(3.30)
$$\left(\frac{h^2}{\gamma}\right)\frac{\partial\mathbf{U}^{l,m}}{\partial t} = \Big[\underline{\boldsymbol{\mathcal{L}}} + \underline{\boldsymbol{\mathcal{K}}}^{l-1,m}\exp\left(-ikh\cos(\theta)\right) + \underline{\boldsymbol{\mathcal{K}}}^{l+1,m}\exp\left(ikh\cos(\theta)\right)$$
$$+ \underline{\boldsymbol{\mathcal{K}}}^{l,m-1}\exp\left(-ikh\sin(\theta)\right) + \underline{\boldsymbol{\mathcal{K}}}^{l,m+1}\exp\left(ikh\sin(\theta)\right)\Big]\mathbf{U}^{l,m}.$$

By differentiating $\mathbf{U}^e$ in (3.30) similar to the 1D analysis, we arrive at an eigenvalue problem with $(p+1)^2$ eigenpairs. The rest of the analysis using both Fourier and *combined-mode* analysis follows the same procedure as in the 1D case with additional DOFs and 2D spatial support. The classical Fourier analysis follows the same method as the one used in Gao, Wang, and Huynh [16], and the minimum eigenvalues computed in this work agree very well with their results.

The 2D analysis has an additional parameter θ wave angle. Due to the nature of the generating periodic pattern, the problem possesses a $\theta = 45°$ symmetry property. If the wave is incident in the x or y directions (quasi 1D wave), then the 2D analysis should recover the 1D analysis exactly. We note that for the analysis in 2D the smallest length scale of the DG method for the grid in Figure 10 remains the same as in the 1D case of $h/(p+1)$. This is valid for initial solutions of the form in (3.22), where the wave is moving in one direction. In this case, the length or distance traveled by the wave through the element $\Omega_{l,m}$ in Figure 10 is equivalent to

(3.31)
$$d_{wave} = h/\max\{\cos(\theta),\sin(\theta)\},$$

and the number of DOFs $(nDOF)_{d_{wave}}$ in the direction of the wave propagation becomes

(3.32)
$$(nDOF)_{d_{wave}} = (p+1)/\max\{\cos(\theta),\sin(\theta)\}.$$

This nondimensionalization parameter is important when trying to compare solutions at different angles θ and to arrive at the performance in 2D for different DG methods for diffusion.
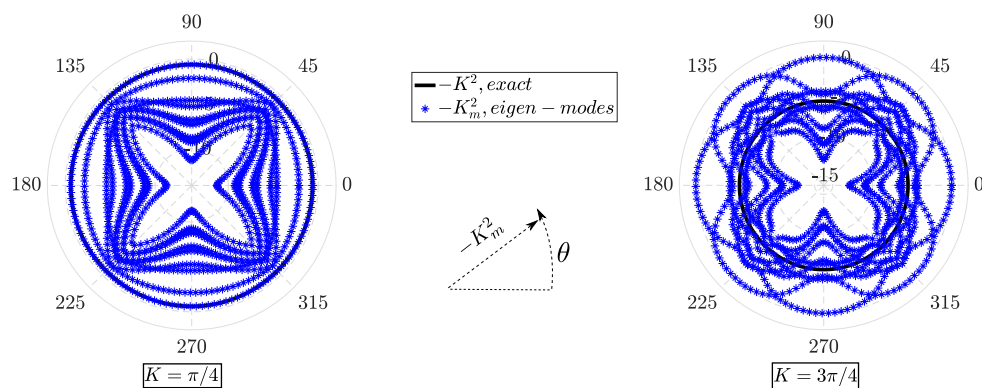
FIG. 11. *Semidiscrete eigenmode dissipation (radial) versus wave incident angle θ (azimuthal) for a $(p+1)^2$ number of eigenvalues of the* **BR2**$p2$-$\eta1$ *in 2D at constant wavenumbers K. The physical-mode is identified as the one that approximates the exact dissipation relation of $-K^2$.*

As an example, we present the classical *eigenmode* analysis results for the **BR2** scheme at a certain K in Figure 11. In this figure the symmetry property is clearly obvious. It is also worth noting that it is very difficult to distinguish *physical-mode* and secondary modes for $K > \pi/3$ as in the 1D cases based on this figure. For this type of mesh the **BR2** is again exactly equivalent to the **SIPG** method. The **CDG** is also similar to the **LDG** if quasi-1D waves are used as initial solutions. For 2D incident waves, the **CDG** is different from the **LDG** method, as it preserves the compactness of the scheme previously shown in 1D, whereas **LDG** is noncompact in 2D. Thus, in this section we compare the **BR2**, and **CDG** as representatives of compact schemes in 2D. Compactness in 2D is very desirable to allow for better sparsity patterns for the linear system resulting from implicit discretization and also for efficient parallel programming on modern architecture [30, 24].

We start by commenting on the minimum magnitude η for stability of the **BR2** and **CDG** schemes in 2D. We confirm that the same 1D limits extend to 2D with $\eta_{min} = p/(p+1)$ for **BR2** and $\eta_{min} = -(2p+1)$. The limits of the **BR2** scheme are sharper than the ones previously derived in [7, 3] of $\eta_{min} = N_{edges}$, where N_{edges} are the number of faces/edges of an element. We note that the difference is related to the fact that in this work we consider a parabolic equation with periodic boundary conditions, whereas in [7, 3] the stability conditions were based on the coercivity of the bilinear form for elliptic problems.

The effect of the penalty parameter η on the *combined-mode* results for the **BR2**p2 scheme in 2D is shown in Figure 12. From this figure, it can be seen that for each η the changes with θ are only noticeable around $45°$, and it is more significant for smaller η's than for larger ones. In particular, the standard $\eta = 1$ for the **BR2** scheme does not show a larger effect of θ on the diffusion behavior, specially at low wavenumbers $K = \pi/4$. We can further explain this by considering the overall diffusion versus wavenumber behavior at several wave angles θ, as shown in Figure 13. This figure confirms the previous observation of limited θ effect on the performance of the **BR2** method in 2D.

We also examine the extension of the previously conducted comparisons of the considered schemes in 1D to the 2D case. We focus on the **BR2** and **CDG** scheme with the same set of η's as in the 1D case. We compare Figures 6 and 7 with Figures 14 and 15 at $\theta = 45°$. From these figures, we can see that this is again an extension of the 1D analysis and proves the applicability of the *combined-mode* results for 2D cases as
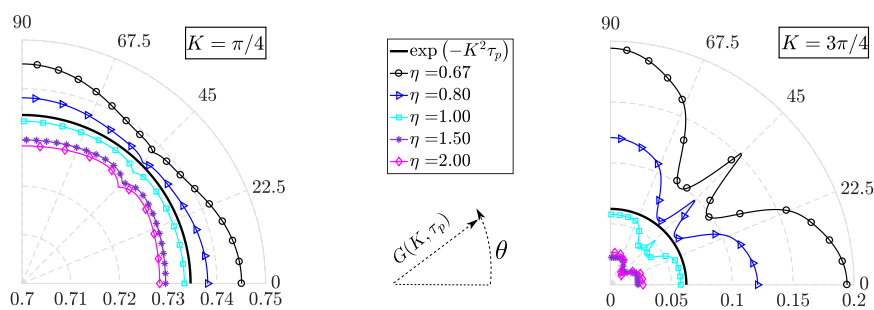
FIG. 12. *Effect of the penalty parameter η on the diffusion factor $G(K, \tau_p)$ (radial) for the* **BR2**p2 *scheme as a function of wave angle θ^o (azimuthal) in 2D at constant wavenumbers K, $\tau_p = 0.5$.*
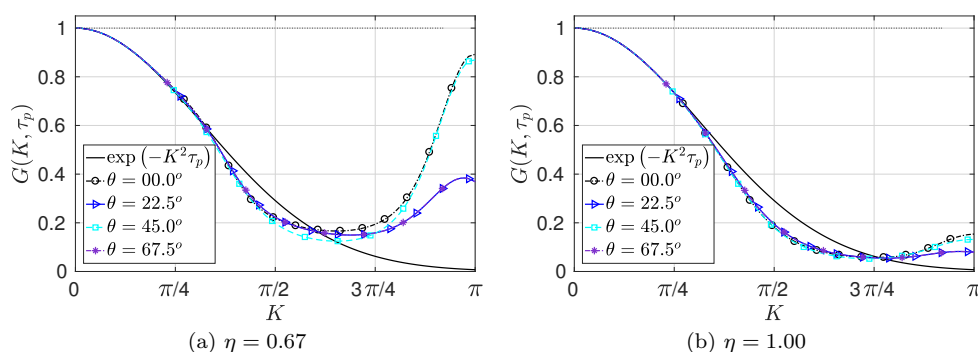

(a) $\eta = 0.67$ (b) $\eta = 1.00$

FIG. 13. *Comparison of the diffusion factors for* **BR2**p2 *schemes at different wave angles θ in 2D, and $\tau_p = 0.5$.*
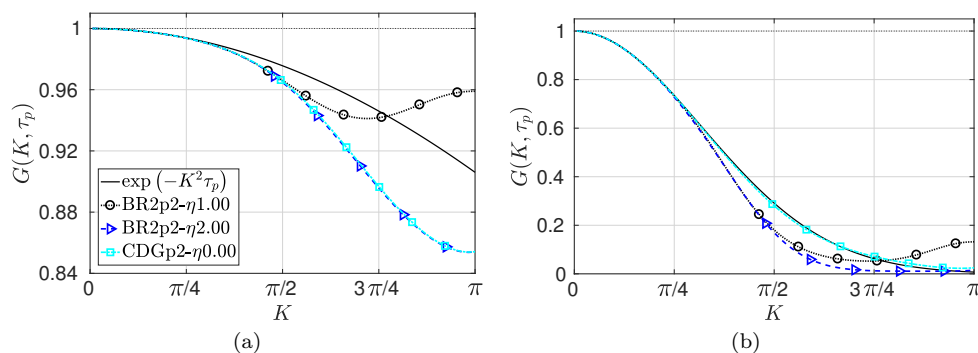

(a)   (b)

FIG. 14. *Comparison of the diffusion behavior of several p2 diffusion schemes for short time $\tau_p = 0.01$ (left) and relatively long time $\tau_p = 0.5$ (right) simulations. These results are for the 2D mesh pattern in Figure 10 at $\theta = 45°$ and are to be compared with Figure 6.*

well. Only slight changes can be noticed when comparing these figures with their 1D counterparts, and the relative behavior between the considered schemes still holds. A further insight can be drawn from Figure 16, where the comparisons are made at constant wavenumbers K. This figure shows that the changes associated with θ are more significant at high wavenumbers for the **CDG** scheme than at low wavenumbers.
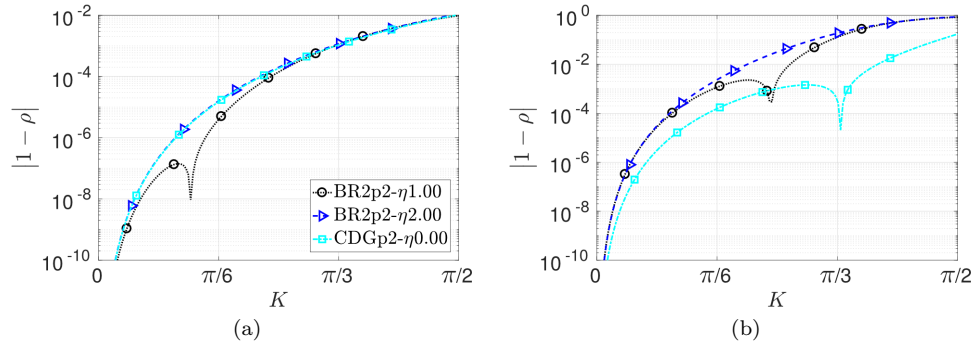
FIG. 15. *Comparison of the diffusion errors of p2 diffusion schemes for short time $\tau_p = 0.01$ (left) and long time $\tau_p = 2.0$ (right) simulations. These results are for the 2D mesh pattern in Figure 10 at $\theta = 45°$ and are to be compared with Figure 7.*
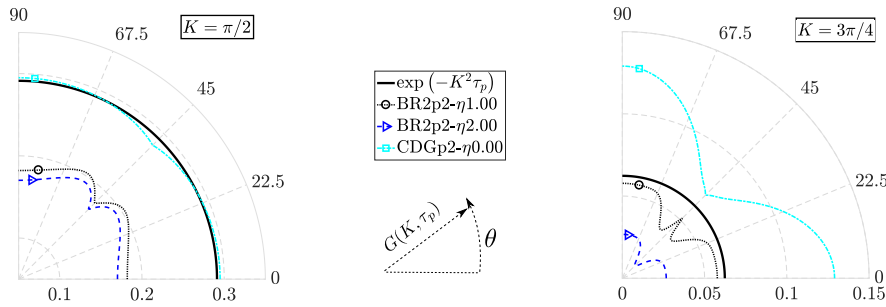

FIG. 16. *Comparison of the diffusion factors of p2 diffusion schemes, $\tau_p = 0.5$, as a function of wave angle $\theta°$ in 2D for constant wavenumbers K.*

4. Numerical tests.

4.1. Linear case of a single frequency wave. In this case, we utilize the same initial condition of (3.1) as is used in the Fourier analysis. The numerical simulation of this initial condition is basically a solution of (2.1) for a sine and a cosine wave. The domain $\mathcal{D}$ is $[0, L]$ and $L = 1$, and we discretize the domain into N_e elements. For a DG scheme, the initial solution is projected using the L_2 projection onto the space $\mathcal{P}^p$ on each cell Ω_e. In this test, we choose a wave with $k = 6\pi$, and Figure 17 shows the p2 projected solutions for two resolutions $N_e = 6, 8$ corresponding to $K = \pi/3, \pi/4$. From this figure we can see that when the resolution is not enough, the two projected solutions of a sine and cosine wave differ significantly, i.e., the case $(K = \pi/3, N_e = 6)$. Indeed, by inspecting the projection of the cosine wave analytically for the $(K = \pi/3)$ case, it turns out that it results in a linear representation. We note that as the resolutions increase (increasing p or N_e), the sine and cosine waves projections become more identical; see, for example, the second case of $(K = \pi/4, N_e = 8)$.

Afterward, we verify the semidiscrete *combined-mode* analysis diffusion error results for $K = \pi/3$ as an example. For viscous fluxes, we consider the same family of schemes used in the analysis comparisons. For time integration, we use the 3-stage Runge–Kutta (RK3) method of third order but with a sufficiently small time-step $\Delta t = 1e-4$ to guarantee being close to the semidiscrete case. For this verification to be consistent, we compute the same average energy/amplitude quantity as in (3.17),
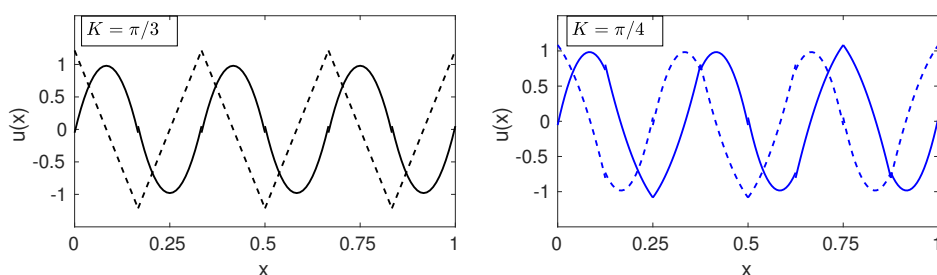
FIG. 17. *Initial p2 projected solution of a single Fourier mode $k = 6\pi$. Note that $N_e = 6$ (left figure), $N_e = 8$ (right figure). Sine wave projections are represented by solid lines, while the cosine ones are dashed lines.*
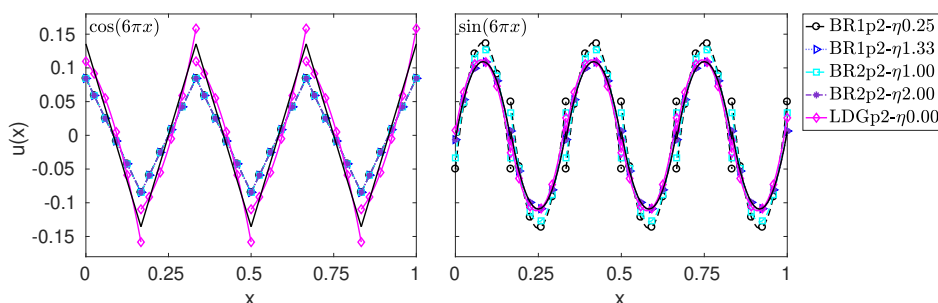

FIG. 18. *Comparison of the simulation of a single Fourier mode ($k = 6\pi$) using several viscous flux formulations and RK3 for time integration. In this figure, $K = \pi/3$, $N_e = 6$, and $\tau_p = 2.0$. The exact DG solution is represented by solid lines without symbols.*

but here it is computed numerically for the whole domain

$$(4.1) \quad E_{num} = \left(\frac{1}{L} \int_0^L \left(u^e(x,t) \right)^2 \, \mathrm{d}x \right)^{1/2} = \left(\sum_{e=0}^{Ne-1} \frac{1}{h_e} \int_{x_{e-1/2}}^{x_{e+1/2}} \left(u^e(x,t) \right)^2 \, \mathrm{d}x \right)^{1/2}.$$

Consequently, the numerical diffusion factor is defined as

$$(4.2) \quad\quad\quad\quad\quad\quad G_{num}(\tau_p) = E_{num}(\tau_p)/E_{init}.$$

In order to compare the results of the *combined-mode* analysis with numerical simulations for such wavenumbers, one should compute the diffusion errors based on the energy of the two sine and cosine waves. In other words, we have a Fourier mode of the form

$$\exp(ikx) = \cos(kx) + i\sin(kx) \rightarrow E_{num} = \sqrt{E_{\cos}^2 + E_{\sin}^2},$$

which is numerically equivalent to the energy definitions in (3.17) and (3.18).

The comparison results for the $K = \pi/3$ case are presented in Table 4. These results can be compared with Figure 7 for the true diffusion error comparison. In addition, the numerical solutions for both the sine and cosine waves are presented in Figure 18. We can see from this figure that indeed the **BR1**p2-η1.33 and **BR2**p2-η2.00 showed identical results for both waves. These results agree well with the analysis results and also with the computed energies in Table 4. These results also show that it is not straightforward to draw conclusions based on the numerical simulations solely. The *combined-mode* analysis helped significantly in quantifying the differences between the considered schemes.

TABLE 4
Comparison of the numerical and combined-mode analysis results for the simulation of a single Fourier-mode $\exp{(ikx)}$ *at* $\tau_p = 2.0$. *This is for the case* $K = \pi/3$, $N_e = 6$ *and the initial projected energy (average amplitude) of this wave* $E_{ex}(k, 0) = 0.9962$.

Scheme	Numerical simulation				*Combined-mode* analysis
	E_{cos}	E_{sin}	E_{tot}	$|1 - \rho|$	$|1 - \rho|$
BR1p2-η0.25	0.0488	0.0939	0.1058	0.0480	0.0476
BR1p2-η1.33	0.0488	0.0792	0.0930	0.1632	0.1634
BR2p2-η1.00	0.0488	0.0887	0.1012	0.0894	0.0889
BR2p2-η2.00	0.0488	0.0792	0.0930	0.1632	0.1634
LDGp2-η0.00	0.0786	0.0803	0.1124	0.0114	0.0110
DG exact solution	0.0789	0.0783	0.1111	–	–

4.1.1. Linear case with a Gaussian profile. In this section we compare the performance of several p2 diffusion schemes coupled with RK3 for a simulation of a broadband Gaussian wave. This helps in quantifying the numerical errors associated with a wide range of wavenumbers for a particular scheme. Consider an initial solution for the linear-heat equation (2.1) of the form

$$(4.3) \qquad u(x, 0) = \exp{(-b\,x^2)}, \quad x \in [-L, L],$$

where $2L$ is the length of the domain, with $L = 1$. The exact solution can be computed analytically using the method of separation of variables for linear PDEs

$$(4.4) \qquad u_{ex}(x, t) = a_0 + \sum_{j=1}^{\infty} a_j \, \cos{(j\pi/L)} \, \exp{(-\gamma\,j^2\,t)},$$

where a_0, a_j are constant coefficients given by

$$(4.5) \qquad \begin{aligned} a_0 &= \frac{\sqrt{\pi}}{2c}, \quad a_j = \frac{\sqrt{\pi}}{c} \, \mathcal{R}e\left(\mathrm{erf}(z_j)\right) e^{-j^2/(4b)}, \\ z_j &= c + i\frac{j\pi}{2c}, \quad c = L\sqrt{b} \end{aligned}$$

and erf(.) is the error function operating on a complex number z. For this case, the parameter $b = 1.5e4$ is chosen to yield a sufficiently smooth case with a wide range of wavenumbers. This results in a very sharp Gaussian wave in the spatial domain, while its Fourier transform is very wide in the frequency space (underresolved case).

Figure 19 displays both the Gaussian wave and the projected initial solution in addition to their fast Fourier transforms (FFT). We note the input to the FFT is a continuous solution on a uniform grid, and this continuous solution is obtained by averaging the interface solutions between two elements in addition to using a large number of points ($>$nDOF) inside each element. This procedure is utilized to converge the FFT results to a unique distribution with minimum errors. However, as we can see from Figure 19, there are still some differences between the Gaussian wave FFT and the projected solution FFT even for $K = 0$. We attribute these differences to both the projection error as well as the error introduced by the jumps at interfaces, which cannot be excluded by averaging.

This test case is simulated using the same group of schemes used in the single frequency wave test and with the same time integration settings. Figure 20 presents the diffusion factor results through numerical simulation for both short and long time simulations. In this case, the wave energy is simply defined as

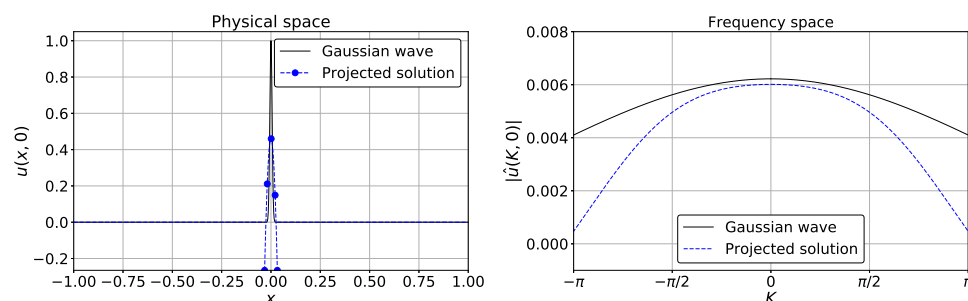$$(4.6) \qquad E\left(K, \tau_p\right) = |\hat{u}\left(K, \tau_p\right)|^2,$$

Fig. 19. *Representation of the initial Gaussian wave solution along with its p2 projection. The left figure shows the initial solution and its projection plotted in the physical domain x, and the right figure shows their FFT frequency domain results.*
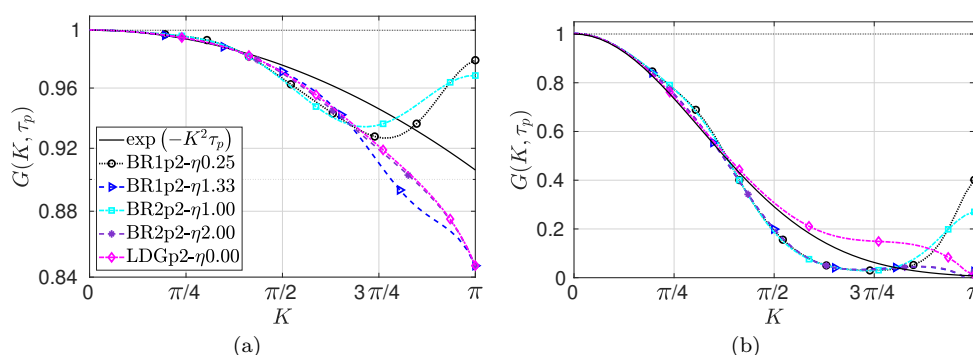

Fig. 20. *Numerical simulation of a Gaussian wave. This figure presents the comparison of the diffusion factors for several p2 spatial schemes coupled with RK3 for $\tau_p = 0.01$ (left) and $\tau_p = 0.5$ (right) and with small $\Delta t = 1e - 4$. This figure is to be compared with Figure 6.*

where $|\hat{u}(K; \tau_p)|$ is the amplitude of the wave as determined by the FFT. The results in Figure 20 show good agreement with the semidiscrete results in Figure 6 for the diffusion factors at $\tau_p = 0.01$, $\tau_p = 0.5$. However, these two sets of figures are not exactly identical. The differences can be attributed to the errors associated with the FFT results as pointed out earlier. Nevertheless, the numerical results provide the same general comparison results between different schemes and hence verify the applicability of the *combined-mode* analysis for assessing the diffusion behavior of DG schemes.

4.2. Viscous Burgers case. Consider the viscous Burgers equation

$$(4.7) \qquad \frac{\partial u}{\partial t} + \frac{\partial F(u)}{\partial x} = \gamma \frac{\partial^2 u}{\partial x^2}, \quad F = u^2/2,$$

where F is the nonlinear inviscid flux function. For a randomly generated velocity distribution from an initial energy spectrum, the solution of this equation undergoes a chaotic (turbulence-like) behavior through time. This case has been used by many researchers to assess the behavior of numerical methods for ILES [28, 33, 2].

In this work, we utilize this case in a slightly different manner than what is usually performed in the literature [12, 2]. That is by requiring a small Péclet (Pe) number in addition to a higher viscosity value of $\gamma = 0.015$ in order to make the

diffusion part of the problem more dominant. Consequently, a direct comparison with the *combined-mode* analysis for diffusion can be established. The Péclet number is defined as $\text{Pe} = Eh/\gamma = u_{rms}h/\gamma$, and E is defined as the total average energy or average amplitude in the domain equation (4.1). Based on this definition it is clear that the Pe will change with time as the velocity distribution changes. Therefore, we focus in this case on long time behavior where the Pe is ensured to be < 1.

The case setup for simulation is similar to [2], where a periodic domain $x \in [0, 2\pi]$ is used with an initial energy spectrum

$$(4.8) \qquad E(k; 0) = E_0(k) = Ak^4 \varrho^5 \exp\left(-k^2 \varrho^2\right),$$

where k is the prescribed wavenumber and (ϱ, A) are constants to control the position of the maximum energy. For $\varrho = 0.1, A = 2/(3\sqrt{\pi})$, the spectrum reaches its maximum at $k = 13$. Assuming a Gaussian distribution in the frequency space, the initial velocity field reads as

$$(4.9) \qquad \hat{v}(k) = \sqrt{2E_0(k)} \, \exp\left(i\Phi(k)\right),$$

where $\Phi(k)$ is a random phase angle that is uniformly distributed in $[0, 2\pi]$ for each wavenumber k. In the physical space, an inverse Fourier transform can be employed to yield a real velocity field, provided that $\Phi(k) = -\Phi(-k)$,

$$(4.10) \qquad v(x) = \sum_{k=0}^{k_{max}} \sqrt{2E_0(k)} \cos\left(kx + 2\pi\Phi(k)\right),$$

where k is the prescribed integer wavenumber with $k_{max} = 2048$.

This initial solution is projected onto the DG space of polynomials of degree at most p using an L_2 projection. For the convection terms we employ a standard DG discretization in space, and Rusanov [36] numerical (upwind) fluxes are used at interfaces. The diffusion terms are discretized by any scheme of the viscous diffusion schemes introduced in subsection 2.3.

We perform simulations for the same group of spatial schemes that were utilized in the previous numerical tests and with the same time integration settings. For all schemes, the Burgers equation (4.7) is solved for a 64 randomly generated samples of the initial velocity field equation (4.10), and then the kinetic energy (KE) spectrum is computed using an ensemble averaged FFT of these samples. The discretization of the domain involves $N_e = 50$ elements, which results in an initial Pe ≈ 2.1 for all simulations. This Pe number quickly decreases with time, allowing for a diffusion-dominated behavior for long time simulations. A DNS simulation was conducted using $N_e = 500$ elements to provide a reference solution for the comparisons.

The KE spectra for the considered schemes at $t = 0.5$ are presented in Figure 21. From this figure, it can be inferred that indeed for long time simulations, the **LDG**-$\eta 0$ scheme is the most accurate in approximating the exact diffusion behavior since it captures more of the KE spectrum than all the other schemes. However, for high wavenumbers it is slightly less dissipative than all the other schemes, but since this is a common behavior for all DG schemes [2], we think that its accuracy outweigh this problem. All the other schemes are comparable in terms of low to moderate wavenumber accuracy despite some differences at high wavenumbers. Indeed, the two equivalent schemes identified through the *combined-mode* analysis show the same behavior for this case as well, namely, schemes **BR1**p2-$\eta 1.33$ and **BR2**p2-$\eta 2$. In
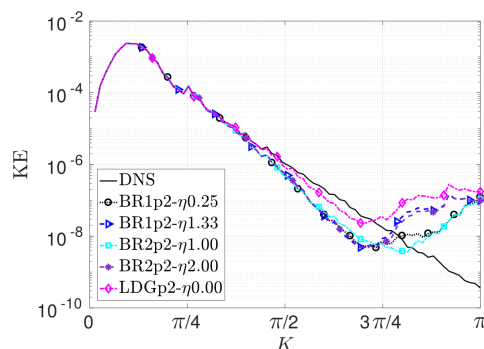
Fig. 21. *Numerical results of the KE spectra for the Burgers turbulence case at $t = 0.5$, $Pe \approx 0.15$. For time integration, the RK3 scheme is utilized, $\Delta t = 1e - 4$ and $nDOF = 150$ for all schemes.*
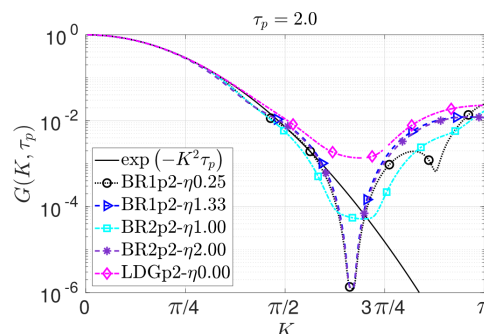

Fig. 22. *Diffusion factors of several $p2$ diffusion schemes through combined-mode analysis. These results are to be compared with Figure 21.*

addition, the **BR1**p2-η0.25 scheme shows a good behavior that is close to the **BR2**p2-η1, proving that it improves the original **BR1**p2-η0 behavior.

These results are in close agreement with the comparisons made using the *combined-mode* analysis in section 3. For instance, in Figure 6(b), we can see that the **LDG**p2-η0 scheme has the best accuracy in comparison with the exact diffusion (which is analogous to the DNS energy spectrum in this Burgers case). Figure 22 also supports these results and shows that the **LDG**p2-η0 has less than exact dissipation at high wavenumbers followed by **BR1**p2-η1.33 and **BR2**p2-η2.0 schemes. This comparison is only qualitatively true since the *combined-mode* analysis results are for a pure (linear) diffusion problem, while this numerical case results are for a viscous nonlinear Burgers case. As a result, neither of Figures 6(b) and 22 correspond to the same point in time as in Figure 21 due to the differences in timescales. Despite these differences, we can clearly see that the *combined-mode* analysis gives accurate and useful predictions about the behavior of DG diffusion schemes in a simple and informative manner.

5. Conclusions. We have presented a new *combined-mode* approach for the diffusion analysis of DG methods applied to the linear heat equation in 1D and 2D. This approach removes the ambiguity related to describing the schemes' behavior based on individual eigenmodes resulted from the classical Fourier analysis technique. It was shown that the classical definition of the *physical-mode* cannot be utilized for studying

the behavior of DG schemes for diffusion problems over the entire wavenumber range and is only limited to $K \leq \pi/3$. The *combined-mode* approach was able to predict accurately the diffusion behavior of DG viscous schemes for the entire wavenumber range. In addition, it has shown that short and long time simulations are very different due to the coupling of the eigenmodes. A comparative diffusion study was also conducted between the considered DG diffusion schemes.

For all the schemes considered in this work, the minimum magnitude of η for stability results in a slower diffusion rate than the exact one, which may lead to unstable behavior for nonlinear cases. These minimum magnitudes of η extend to 2D for all the considered schemes. Adjusting the penalty parameter η was shown to have a strong influence on the scheme behavior for short time simulations. By comparing the considered schemes, we were able to show that the **LDG**-$\eta0$ method in 1D and **CDG**-$\eta0$ in 2D have the best accuracy in approximating the exact diffusion behavior, especially for long time simulations in addition to a slower rate of increase for the diffusion error. For short time simulations, we were able to adjust the penalty parameter of the **BR1**p2 and the **BR2**p2 schemes, ($\eta^{br1} = 1.33$, $\eta^{br2} = 2.0$), to have similar performance to the **LDG**p2-$\eta0$ for low wavenumbers. We note that for other orders these values are different; for instance, for p5 we can choose $\eta^{br1} = 0.8$, $\eta^{br2} = 1.65$ to achieve similar performances.

In 2D, the effect of the wave incidence angle is more significant for high wavenumbers, long time simulations, as well as smaller η close to the stability limits. For low wavenumber and well-resolved waves the behavior is only slightly dependent on the wave angle. The *combined-mode* analysis results were verified using several numerical test cases.

Appendix A. Properties of Legendre polynomials.   In this work, test and basis functions are chosen to be the Legendre polynomials. For the sake of completeness, we mention the relevant properties of these polynomials in this article as in [31].

Property A.1.

$$\phi_l(1) = 1 \qquad \text{and} \qquad \phi_l(-1) = (-1)^l. \tag{A.1}$$

Property A.2.

$$\int_{-1}^{1} \phi_l \phi_j \mathrm{d}\xi = \frac{2}{2l+1} \delta_{lj}, \text{ where } \delta_{lj} \text{ is the Kronecker delta.} \tag{A.2}$$

Property A.3.

$$\int_{-1}^{1} \frac{\partial \phi_l}{\partial \xi} \frac{\partial \phi_j}{\partial \xi} \mathrm{d}\xi = \begin{cases} 2 \times \mathrm{mod}\,(l+j, 2), & j < l, \\ 0 & \text{otherwise.} \end{cases} \tag{A.3}$$

Appendix B. Equivalence between the SIPG and BR2.

LEMMA B.1. *The lifting operator* $r^e(\llbracket u \rrbracket)(\xi)$ *employed in the stabilization term* $\alpha(\llbracket u \rrbracket)$ *of the* **BR2** *method is equivalent to the following polynomial:*

$$r_f^e(\llbracket u \rrbracket)(\xi) = -\frac{1}{2h} \llbracket u \rrbracket_f \sum_{l=0}^{p} (2l+1)\, \phi_l(\xi)\, \phi_l\big|_f. \tag{B.1}$$

Proof. The lifting operator r_f^e is a polynomial of degree p on Ω_e defined for each face f as

$$(B.2) \qquad r_f^e(\llbracket u \rrbracket)(\xi) = \sum_{j=0}^{p} r_{f,j}^e \, \phi_j(\xi).$$

Using the definition of r_f^e in (2.20), we can write for each test function ϕ_l, $l = 0, \dots, p$,

$$(B.3) \quad -\frac{1}{2} \llbracket u \rrbracket_f \phi_l \big|_f = \int_{\Omega_e} r_f^e(\llbracket u \rrbracket) \phi_l \, \mathrm{d}x = \frac{h}{2} \int_{\Omega_s} r_f^e(\llbracket u \rrbracket) \phi_l \, \mathrm{d}\xi = \frac{h}{2} \sum_{j=0}^{p} r_{f,j}^e \int_{-1}^{1} \phi_j \phi_l \, \mathrm{d}\xi,$$

and using the Property A.2 of the Legendre polynomials,

$$(B.4) \qquad -\frac{1}{2} \llbracket u \rrbracket_f \phi_l \big|_f = \frac{h}{2} \sum_{j=0}^{p} \frac{2}{2j+1} \delta_{lj} \, r_{f,j}^e = \frac{h}{2l+1} \, r_{f,l}^e,$$

and as a result,

$$(B.5) \qquad r_{f,l}^e = -\frac{1}{2h} \llbracket u \rrbracket_f \, (2l+1) \, \phi_l \big|_f,$$

and by substituting in (B.2) we complete the *proof.* □

THEOREM B.2. *The* **SIPG** *method is equivalent to the* **BR2** *in* $1D$ *if and only if*

$$(B.6) \qquad C(p) = \frac{(p+1)^2}{2} \qquad and \qquad \eta^{br2} = \eta^{sipg}.$$

Proof. The only difference between the **SIPG** and **BR2** schemes is the definition of the stabilization term $\alpha(\llbracket u \rrbracket)$ in the numerical flux $\hat{\Theta}$. For the **SIPG** this is defined as $(\eta^{sipg} \llbracket u \rrbracket / h) \, C(\mathrm{p})$, where for the **BR2** it is $-\eta^{br2} \{\!\{ r_f^e(\llbracket u \rrbracket) \}\!\}$. We simply choose $\eta = \eta^{br2} = \eta^{sipg}$, and we only prove the theorem for $C(p) = (p+1)^2/2$.

Lemma B.1 yields

$$(B.7) \qquad \begin{aligned} \{\!\{ r_f^e(\llbracket u \rrbracket) \}\!\} &= \frac{1}{2} \left(r_f^-(\llbracket u \rrbracket) + r_f^+(\llbracket u \rrbracket) \right) \\ &= \frac{1}{2} \left(-\frac{1}{2h} \llbracket u \rrbracket \sum_{l=0}^{\mathrm{p}} (2l+1) \left(\phi_l^-(1) \, \phi_l^-(1) + \phi_l^+(-1) \, \phi_l^+(-1) \right) \right), \end{aligned}$$

and using the Property A.1 of the Legendre polynomials,

$$(B.8) \qquad \{\!\{ r_f^e(\llbracket u \rrbracket) \}\!\} = \frac{1}{2} \left(-\frac{1}{2h} \llbracket u \rrbracket \sum_{l=0}^{\mathrm{p}} (2l+1)(1+1) \right) = -\frac{1}{2h} \llbracket u \rrbracket \sum_{l=0}^{\mathrm{p}} (2l+1),$$

and the sum of the arithmetic series of odd numbers,

$$(B.9) \qquad \sum_{l=0}^{\mathrm{p}} (2l+1) = 1 + 3 + 5 + \cdots = (\mathrm{p}+1)^2,$$

we get

$$(B.10) \qquad \{\!\{ r_f^e(\llbracket u \rrbracket) \}\!\} = -\frac{\llbracket u \rrbracket}{h} \frac{(p+1)^2}{2}.$$

Finally, we have

$$\alpha^{br2}(\llbracket u \rrbracket) = \alpha^{sipg}(\llbracket u \rrbracket)$$

$$\Longleftrightarrow \qquad -\eta \{\!\!\{ r_f^e(\llbracket u \rrbracket) \}\!\!\} = \eta \frac{\llbracket u \rrbracket}{h} C(p)$$

(B.11) $\qquad \Longleftrightarrow \qquad \eta \frac{\llbracket u \rrbracket}{h} \frac{(p+1)^2}{2} = \eta \frac{\llbracket u \rrbracket}{h} C(p)$

$$\Longleftrightarrow \qquad C(p) = \frac{(p+1)^2}{2}. \qquad \qquad \square$$

Appendix C. Detailed expressions for the BR1 method.

LEMMA C.1. *The global lifting operator $R^e(\llbracket u \rrbracket)$ of the* **BR1** *and* **BR2/SIPG** *methods, defined on any element Ω_e, is equivalent to the following polynomial:*

(C.1) $\qquad R^e(\llbracket u \rrbracket) = -\frac{1}{2h_e} \sum_{l=0}^{p} (2l+1) \sum_{f \in \partial\Omega_e} \llbracket u \rrbracket\big|_f \, \phi_l\big|_f \, \phi_l(\xi).$

Proof. Using (2.16) and (2.20) we can see that it is also related to the local lifting operator r_f^e of the **BR2** method in (B.1) as follows:

(C.2) $\qquad R^e(\llbracket u \rrbracket) = \sum_{f \in \partial\Omega_e} r_f^e(\llbracket u \rrbracket)(\xi).$

Using Lemma B.1, we complete the proof. $\qquad \square$

LEMMA C.2. *The averages of the global lifting operator $R^e(\llbracket u \rrbracket)$ of the* **BR1** *and* **BR2/SIPG** *methods, at the interfaces of any element Ω_e, take the forms*

(C.3a) $\qquad \{\!\!\{ R^e(\llbracket u \rrbracket) \}\!\!\}_{e\pm 1/2} = -\frac{C(p)}{h} \llbracket u \rrbracket_{e\pm 1/2} + \frac{C1(p)}{h} \left(\llbracket u \rrbracket_{e\pm 3/2} + \llbracket u \rrbracket_{e\mp 1/2} \right),$

where

(C.3b) $\qquad C(p) = \frac{(p+1)^2}{2} \qquad and \qquad C1(p) = (-1)^{p+1} \frac{(p+1)}{4}.$

Proof. Using Lemma C.1 and Property A.1 of the Legendre polynomials,

(C.4)
$$R^-\big|_{e\pm 1/2} = -\frac{1}{2h} \sum_{l=0}^{p} (2l+1) \left(\llbracket u \rrbracket\big|_{e\pm 1/2} \phi_l^-(\pm 1) + \llbracket u \rrbracket\big|_{e\mp 1/2} \phi_l^-(\mp 1) \right) \phi_l^-(\pm 1)$$
$$= -\frac{1}{2h} \sum_{l=0}^{p} (2l+1) \left(\llbracket u \rrbracket\big|_{e\pm 1/2} + (-1)^l \llbracket u \rrbracket\big|_{e\mp 1/2} \right)$$

and similarly

(C.5)
$$R^+\big|_{e\pm 1/2} = -\frac{1}{2h} \sum_{l=0}^{p} (2l+1) \left(\llbracket u \rrbracket\big|_{e\pm 3/2} \phi_l^+(\pm 1) + \llbracket u \rrbracket\big|_{e\pm 1/2} \phi_l^+(\mp 1) \right) \phi_l^+(\mp 1)$$
$$= -\frac{1}{2h} \sum_{l=0}^{p} (2l+1) \left((-1)^l \llbracket u \rrbracket\big|_{e\pm 3/2} + \llbracket u \rrbracket\big|_{e\pm 1/2} \right).$$

As a result,

(C.6)

$$
\{\!\{R^e\}\!\}_{e\pm1/2} = \frac{1}{2}\left(R^- + R^+\right)\big|_{e\pm1/2}
$$

$$
= -\frac{1}{4h}\sum_{l=0}^{p}(2l+1)\left(2[\![u]\!]\big|_{e\pm1/2} + (-1)^l\left([\![u]\!]\big|_{e\pm3/2} + [\![u]\!]\big|_{e\mp1/2}\right)\right).
$$

Similar to (B.9), note that the sum of alternating arithmetic series of odd numbers

(C.7)
$$
\sum_{l=0}^{p}(2l+1)(-1)^l = 1 - 3 + 5 + \cdots = (-1)^p(p+1)
$$

and consequently

(C.8)

$$
\{\!\{R^e([\![u]\!])\}\!\}_{e\pm1/2} = -\frac{(p+1)^2}{2h}[\![u]\!]\big|_{e\pm1/2} + (-1)^{p+1}\frac{(p+1)}{4h}\left([\![u]\!]\big|_{e\pm3/2} + [\![u]\!]\big|_{e\mp1/2}\right).
$$

This completes the proof. □

REFERENCES

[1] M. AINSWORTH, *Dispersive and dissipative behaviour of high order discontinuous Galerkin finite element methods*, J. Comput. Phys., 198 (2004), pp. 106–130.

[2] M. ALHAWWARY AND Z. J. WANG, *Fourier analysis and evaluation of DG, FD and compact difference methods for conservation laws*, J. Comput. Phys., 373 (2018), pp. 835–862.

[3] D. ARNOLD, F. BREZZI, B. COCKBURN, AND L. MARINI, *Unified analysis of discontinuous Galerkin methods for elliptic problems*, SIAM J. Numer. Anal., 39 (2002), pp. 1749–1779.

[4] K. ASTHANA AND A. JAMESON, *High-order flux reconstruction schemes with minimal dispersion and dissipation*, J. Sci. Comput., 62 (2015), pp. 913–944.

[5] F. BASSI AND S. REBAY, *A high-order accurate discontinuous finite element method for the numerical solution of the compressible Navier–Stokes equations*, J. Comput. Phys., 131 (1997), pp. 267–279.

[6] F. BASSI, S. REBAY, G. MARIOTTI, S. PEDINOTTI, AND M. SAVINI, *A higher-order accurate discontinuous finite element method for inviscid and viscous turbomachinery flows*, in Proceedings of 2nd European Conference on Turbomachinery-Fluid Dynamics and Thermodynamics, R. Decuypere and G. Dibelius, eds., Technologisch Instituut, Antwerp, Belgium, 1997, pp. 99–108.

[7] F. BREZZI, G. MANZINI, D. MARINI, P. PIETRA, AND A. RUSSO, *Discontinuous Galerkin approximations for elliptic problems*, Numer. Methods Partial Differential Equations, 16 (2000), pp. 365–378.

[8] P. CASTILLO, *Performance of discontinuous Galerkin methods for elliptic PDEs*, SIAM J. Sci. Comput., 24 (2002), pp. 524–547.

[9] P. CASTONGUAY, D. M. WILLIAMS, P. E. VINCENT, AND A. JAMESON, *Energy stable flux reconstruction schemes for advection-diffusion problems*, Comput. Methods Appl. Mech. Engrg., 267 (2013), pp. 400–417.

[10] B. COCKBURN AND C.-W. SHU, *The local discontinuous Galerkin method for time-dependent convection-diffusion systems*, SIAM J. Numer. Anal., 35 (1998), pp. 2440–2463.

[11] B. COCKBURN AND C.-W. SHU, *Runge–Kutta discontinuous Galerkin methods for convection-dominated problems*, J. Sci. Comput., 16 (2001), pp. 173–261.

[12] G. DE STEFANO AND O. V. VASILYEV, *Sharp cutoff versus smooth filtering in large eddy simulation*, Phys. Fluids, 14 (2002), pp. 362–369.

[13] J. DOUGLAS AND T. DUPONT, *Interior penalty procedures for elliptic and parabolic Galerkin methods*, in Computing Methods in Applied Sciences, Lecture Notes in Physics, Springer, Berlin, 1976, pp. 207–216.

[14] Y. EPSHTEYN AND B. RIVIÈRE, *Estimation of penalty parameters for symmetric interior penalty Galerkin methods*, J. Comput. Appl. Math., 206 (2007), pp. 843–872.

[15] P. Fernandez, R. C. Moura, G. Mengaldo, and J. Peraire, *Non-modal analysis of spectral element methods: Towards accurate and robust large-eddy simulations*, Comput. Methods Appl. Mech. Engrg., 346 (2019), pp. 43–62.

[16] H. Gao, Z. J. Wang, and H. T. Huynh, *Differential formulation of discontinuous Galerkin and related methods for the Navier-Stokes equations*, Commun. Comput. Phys., 13 (2013), pp. 1013–1044.

[17] G. Gassner and D. A. Kopriva, *A comparison of the dispersion and dissipation errors of Gauss and Gauss–Lobatto discontinuous Galerkin spectral element methods*, SIAM J. Sci. Comput., 33 (2011), pp. 2560–2579.

[18] G. J. Gassner, A. R. Winters, F. J. Hindenlang, and D. A. Kopriva, *The BR1 scheme is stable for the compressible Navier–Stokes equations*, J. Sci. Comput., (2018), pp. 1–47.

[19] W. Guo, X. Zhong, and J.-M. Qiu, *Superconvergence of discontinuous Galerkin and local discontinuous Galerkin methods: Eigen-structure analysis based on Fourier approach*, J. Comput. Phys., 235 (2013), pp. 458–485.

[20] R. Hartmann and P. Houston, *Symmetric interior penalty DG methods for the compressible Navier-Stokes equations* I: *Method formulation*, Int. J. Numer. Anal. Model., 3 (2006), pp. 1–20.

[21] J. S. Hesthaven and T. Warburton, *Nodal Discontinuous Galerkin Methods: Algorithms, Analysis, and Applications*, 1st ed., Springer, Berlin, 2010.

[22] F. Q. Hu, M. Y. Hussaini, and P. Rasetarinera, *An analysis of the discontinuous Galerkin method for wave propagation problems*, J. Comput. Phys., 151 (1999), pp. 921–946.

[23] H. T. Huynh, *A reconstruction approach to high-order schemes including discontinuous Galerkin for diffusion*, in 47th AIAA Aerospace Sciences Meeting, AIAA 2009-403, AIAA, Reston, VA, 2009.

[24] H. T. Huynh, Z. J. Wang, and P. E. Vincent, *High-order methods for computational fluid dynamics: A brief review of compact differential formulations on unstructured grids*, Comput. Fluids, 98 (2014), pp. 209–220.

[25] R. Kannan and Z. J. Wang, *A study of viscous flux formulations for a p-multigrid spectral volume Navier-Stokes solver*, J. Sci. Comput., 41 (2009), p. 165.

[26] P. Lasaint and P. A. Raviart, *On a finite element method for solving the neutron transport equation*, in Mathematical Aspects of Finite Elements in Partial Differential Equations, C. de Boor, ed., Academic Press, New York, 1974, pp. 89–123.

[27] B. V. Leer and S. Nomura, *Discontinuous Galerkin for diffusion*, in the 17th AIAA Computational Fluid Dynamics Conference, AIAA 2005-5108, AAIA, Reston, VA, 2005.

[28] Y. Li and Z. J. Wang, *A priori and a posteriori evaluations of sub-grid scale models for the Burgers' equation*, Comput. Fluids, 139 (2016), pp. 92–104.

[29] R. C. Moura, S. J. Sherwin, and J. Peiró, *Linear dispersion-diffusion analysis and its application to under-resolved turbulence simulations using discontinuous Galerkin spectral/hp methods*, J. Comput. Phys., 298 (2015), pp. 695–710.

[30] J. Peraire and P. Persson, *The compact discontinuous Galerkin (CDG) method for elliptic problems*, SIAM J. Sci. Comput., 30 (2008), pp. 1806–1824.

[31] S. Quaegebeur, S. Nadarajah, F. Navah, and P. Zwanenburg, *Stability of energy stable flux reconstruction for the diffusion problem using compact numerical fluxes*, SIAM J. Sci. Comput., 41 (2019), pp. A643–A667.

[32] W. H. Reed and T. R. Hill, *Triangular Mesh Methods for the Neutron Transport Equation*, Technical report LA-UR–73-479; CONF-730414–2, Los Alamos Scientific Laboratory, Los Alamos, NM, 1973.

[33] O. San, *Analysis of low-pass filters for approximate deconvolution closure modelling in one-dimensional decaying Burgers turbulence*, Int. J. Comput. Fluid Dyn., 30 (2016), pp. 20–37.

[34] K. Shahbazi, *An explicit expression for the penalty parameter of the interior penalty method*, J. Comput. Phys., 205 (2005), pp. 401–407.

[35] C.-W. Shu, *High order WENO and DG methods for time-dependent convection-dominated PDEs: A brief survey of several recent developments*, J. Comput. Phys., 316 (2016), pp. 598–613.

[36] E. F. Toro, *Riemann Solvers and Numerical Methods for Fluid Dynamics*, Springer, Berlin, 2009.

[37] B. C. Vermeire and P. E. Vincent, *On the behaviour of fully-discrete flux reconstruction schemes*, Comput. Methods Appl. Mech. Engrg., 315 (2017), pp. 1053–1079.

[38] R. Vichnevetsky and J. Bowles, *Fourier Analysis of Numerical Approximations of Hyperbolic Equations*, Studies in Applied and Numerical Mathematics, SIAM, Philadelphia, 1982.

[39] Z. J. WANG, *High-order methods for the Euler and Navier–Stokes equations on unstructured grids*, Prog. Aerosp. Sci., 43 (2007), pp. 1–41.

[40] Z. J. WANG AND H. GAO, *A unifying lifting collocation penalty formulation including the discontinuous Galerkin, spectral volume/difference methods for conservation laws on mixed grids*, J. Comput. Phys., 228 (2009), pp. 8161–8186.

[41] H. YANG, F. LI, AND J. QIU, *Dispersion and dissipation errors of two fully discrete discontinuous Galerkin methods*, J. Sci. Comput., 55 (2013), pp. 552–574.

[42] M. ZHANG AND C.-W. SHU, *An analysis of three different formulations of the discontinuous Galerkin method for diffusion equations*, Math. Models Methods Appl. Sci., 13 (2003), pp. 395–413.

[43] M. ZHANG AND J. YAN, *Fourier type error analysis of the direct discontinuous Galerkin method and its variations for diffusion equations*, J. Sci. Comput., 52 (2012), pp. 638–655.